

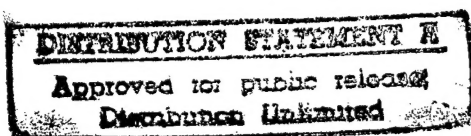
Contract Report SL-96-3
UAST-CR-94-007

JOINT U.S./ROK R&D PROGRAM FOR NEW UNDERGROUND AMMUNITION STORAGE TECHNOLOGIES

FINAL REPORT MATERIAL CHARACTERIZATION OF SAMPLES FROM THE LINCHBURG MINE

by

19961120 048



J. Wesley Martin

TerraTek, Inc.
P.O. Box 8275
Salt Lake City, UT 84108-8275

September 1996

Prepared for U.S. Army Engineer Waterways Experiment Station
3909 Halls Ferry Road
Vicksburg, Mississippi 39180-6199

DTIC QUALITY INSPECTED 1

The contents of this report are not to be used for advertising, publication, or promotional purposes. Citation of trade names does not constitute an official endorsement or approval of the use of such commercial products.



PRINTED ON RECYCLED PAPER

Material Characterization of Samples from the Linchburg Mine

by **J. Wesley Martin**

**TerraTek, Inc.
P. O. Box 8275
Salt Lake City, Utah 84108-8275**

Final report

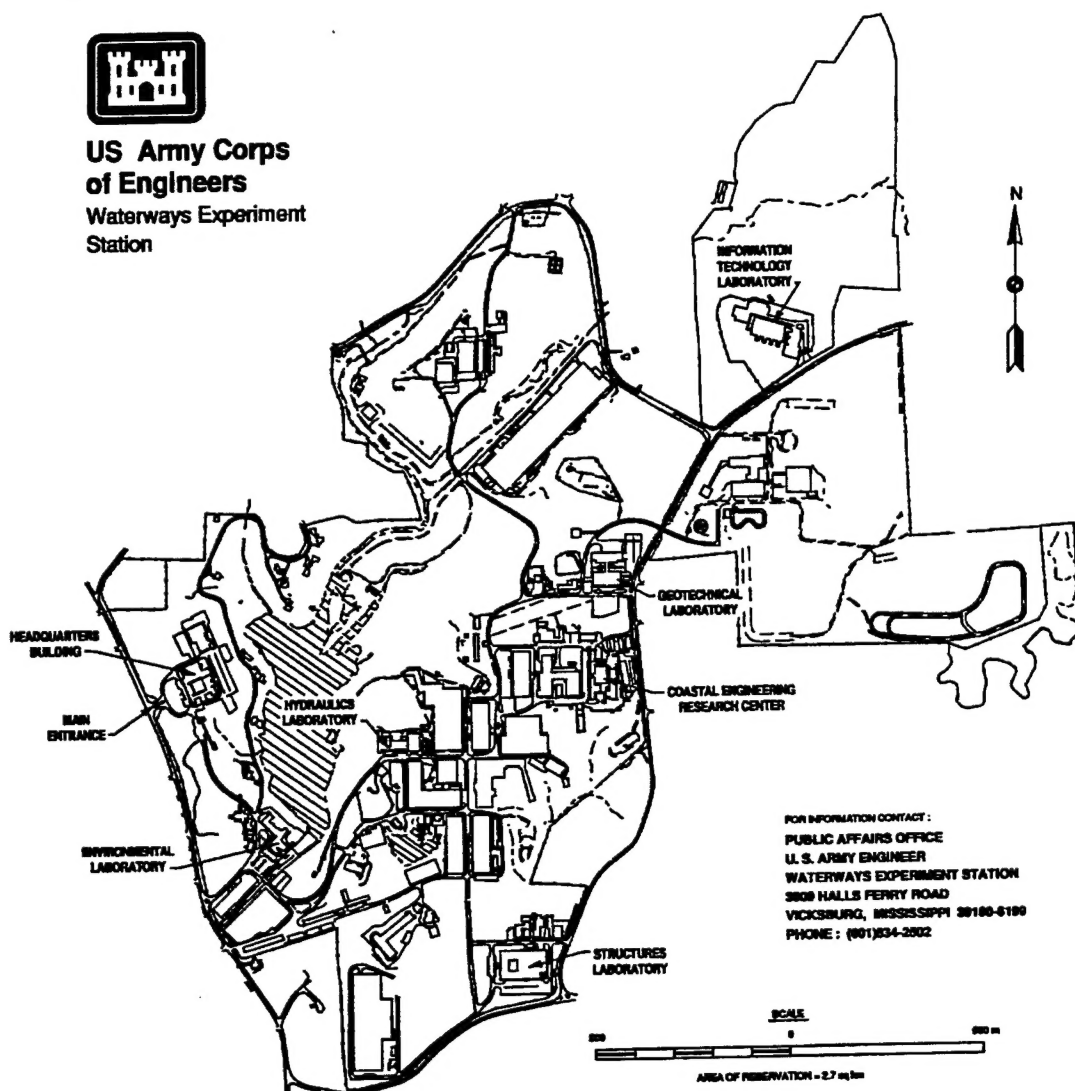
Approved for public release; distribution is unlimited

**Prepared for U.S. Army Corps of Engineers
Washington, DC 20314-1000**

**Monitored by U.S. Army Engineer Waterways Experiment Station
3909 Halls Ferry Road, Vicksburg, MS 39180-6199**



**US Army Corps
of Engineers**
Waterways Experiment
Station



Waterways Experiment Station Cataloging-in-Publication Data

Martin, J. Wesley.

Material characterization of samples from the Lynchburg Mine / by J. Wesley Martin ; prepared for U.S. Army Corps of Engineers ; monitored by U.S. Army Engineer Waterways Experiment Station.

82 p. : ill. ; 28 cm. — (Contract report ; SL-96-3)

"UAST-CR-94-007"—Cover.

Includes bibliographical references.

1. Limestone — New Mexico — Magdalena — Testing. 2. Lynchburg Mine (N.M.) 3. Mines and mineral resources — New Mexico — Magdalena — Testing. 3. Rocks, Carbonate — New Mexico — Testing.
 - I. United States. Army. Corps of Engineers. II. U.S. Army Engineer Waterways Experiment Station. III. Structures Laboratory (U.S. Army Engineer Waterways Experiment Station) IV. Joint U.S./ROK R&D Program for New Underground Ammunition Storage Technologies. V. Title.
 - VI. Series: Contract report (U.S. Army Engineer Waterways Experiment Station) ; SL-96-3.
- TA7 W34c no.SL-96-3

TABLE OF CONTENTS

Section	Page
LIST OF FIGURES	ii
LIST OF TABLES	iii
PREFACE	iv
1 INTRODUCTION	1
1.1 BACKGROUND	1
1.2 SCOPE AND SUMMARY OF INVESTIGATIONS	1
2 CORE RECEIPT AND PREPARATION	5
3 RESULTS	6
3.1 XRD MINERAL AND LITHOLOGY	6
3.2 PHYSICAL PROPERTY RESULTS	7
3.3 MECHANICAL PROPERTIES	7
4 DISCUSSION	15
4.1 MINERAL AND LITHOLOGY	15
4.2 PHYSICAL PROPERTIES	15
4.3 ULTRASONIC VELOCITIES	17
4.4 UNCONFINED COMPRESSION RESULTS	20
4.5 UNIAXIAL STRAIN RESULTS	22
Appendix	
A TEST SAMPLE IDENTIFICATION AND INITIAL CONDITION	A-1
B THIN SECTION MICROGRAPHS AND DESCRIPTIONS	B-1
C TEST PROCEDURES	C-1
D STRESS-STRAIN PLOTS - UNCONFINED COMPRESSION TESTS	D-1
E UNIAXIAL STRAIN GRAPHICAL PRESENTATIONS	E-1

LIST OF FIGURES

Figure	Page
3-1 XRD mineralogic profile for selected Linchburg Mine samples	7
4-1 Dry bulk density comparison of samples from the Linchburg Mine	16
4-2 Porosity comparison for samples from the Linchburg Mine	18
4-3 P-wave velocities for material from the Linchburg Mine	18
4-4 S-wave velocities for material from the Linchburg Mine	19
4-5 Unconfined compressive strengths for material from the Linchburg Mine . . .	21

LIST OF TABLES

Table	Page
1-1 Summary of Laboratory Test Program Conducted on Selected Core Samples from the Linchburg Mine	3
3-1 Summary of XRD Mineralogy of Selected Samples from the Linchburg Mine .	6
3-2 Summary of Physical Properties of Material from the Linchburg Mine	8
3-3 Summary of Physical Properties of Material from the Linchburg Mine	9
3-4 Summary of Ultrasonic Velocities and Dynamic Mechanical Properties	10
3-5 Summary of Ultrasonic Velocities and Dynamic Mechanical Properties	11
3-6 Unconfined Compressive Strength and Static Moduli of Samples from the Linchburg Mine	12
3-7 Summary of Strength Characteristics Determined from Uniaxial Strain Tests .	13
3-8 Summary of Moduli Determined from Uniaxial Strain Tests	14

PREFACE

This study was conducted for the U.S. Army Engineer Waterways Experiment Station (WES) under contract DACA39-92-R-0063 as part of the U.S./Republic of Korea R&D Study for New Underground Ammunition Storage Technologies. Technical managers for the Joint Program were Mr. Landon K. Davis, Geomechanics and Explosion Effects Division (GEED), WES, and Dr. So-young Song, Korean Agency for Defense Development. The Program Managers were Mr. Gary W. Abrisz, U.S. Army Technical Center for Explosives Safety, and COL Yeon Woo Chung, Logistics Bureau, Korean Ministry of Defense.

Mr. J. Wesley Martin, TerraTek, Inc, conducted the study reported herein and is the author of this report. The work was monitored by Mr. Charles E. Joachim, GEED, Structures Laboratory (SL), WES. Dr. Jimmy P. Balsara was Chief, GEED, and Mr. Bryant Mather was Director, SL.

At the time of preparation of this report, Director of WES was Dr. Robert W. Whalin. Commander was COL Bruce K. Howard, EN.

The contents of this report are not to be used for advertising, publication, or promotional purposes. Citation of trade names does not constitute an official endorsement or approval of the use of such commercial products.

SECTION I

INTRODUCTION

1.1 BACKGROUND.

The Joint ROK U.S. R&D Program for New Underground Ammunition Storage Technologies was established in 1991 as a 5-year cooperative research effort between the United States (U.S.) and the Republic of Korea (ROK). The purpose of the program is to develop new design concepts for underground ammunition storage facilities that will significantly reduce the hazard distances and areas presently proscribed for ammunition storage sites by U.S. Department of Defence (DoD) and ROK Ministry of National Defense (MND) safety regulations.

An extensive series of small-scale experiments and computer model calculations was conducted in the U.S. and Korea under the joint R&D program to evaluate the effects of various underground magazine design features on the external blast effects. Based on the results of these efforts, each country conducted a series of intermediate-scale tests, using tunnels and storage chambers excavated in rock, to further study the most promising design features. The U.S. intermediate-scale tests were conducted at 1/3-scale in an inactive mine complex, named the Linchburg Mine, located near Magdalena, NM. This report describes investigations performed by TerraTek, Inc. to characterize the material properties of the rock medium in the test area of the Linchburg Mine.

1.2 SCOPE AND SUMMARY OF INVESTIGATIONS.

Laboratory tests were conducted on predominantly limestone core samples from the Linchburg mine. The core samples were retrieved from horizontal drill holes located in test chambers and drifts. Tests were conducted on thirteen core intervals to characterize the material. This included lithologic descriptions, physical property measurements, ultrasonic velocity measurements, uniaxial compression tests, and uniaxial strain tests. These tests were performed on plug specimens oriented both parallel and perpendicular with respect to the whole core axis. This was done to assess the degree of anisotropic behavior in strata in the

test region. X-Ray Diffraction (XRD) analysis, to determine semi-quantitative mineralogy, was also performed on eight of the thirteen core samples. The laboratory test program, including the individual test sample location and orientation, is summarized in Table 1-1.

The majority of the test samples identified in Table 1-1 are limestones and fractured cherts. In many instances, combinations of chert and carbonate in various proportions were observed in the test specimens. Core sample #5 was a laminated silty mudstone/shale containing no carbonates and was the only sample of this rock type tested. Appendix A presents a brief lithologic description for all of the test plugs, including sample pre-test conditions (e. g ., fractures, bedding, homogeneity). Excluding core sample #5, the mineralogy for all the test samples was dominately calcite and quartz. The samples are exceptionally dense with dry bulk densities averaging $2.69 \text{ Mg/m}^3 (\pm 0.04 \text{ Mg/m}^3)$. As expected for dense carbonate rocks, effective porosities are low, averaging less than 0.5%. Compressional (P) wave velocities averaged $5.39 \text{ km/s} (\pm 0.31 \text{ km/s})$ and shear (S) wave velocities averaged approximately $3.18 \text{ km/s} (\pm 0.26 \text{ km/s})$. Unconfined compressive strengths varied from 53.6 to 195.5 Mpa. Overall, significant mechanical and physical property differences were not determined between the two orientations, suggesting very limited anisotropy.

Table 1-1. Summary of Laboratory Test Program Conducted on the Selected Core Samples from the Lynchburg Mine

Core ID	Test Chamber	Hole #	Test Plug ID ¹	Physical Properties	Ultrasonic Velocities	Unconfined Compression	Uniaxial Strain	XRD	Thin Section
1	4	2	1A-	✓	✓	✓		✓	✓
			1B-	✓	✓		✓		
			1C-⊥	✓	✓	✓			
2	4	2	2A-	✓	✓		✓		
			2B-	✓	✓	✓			
			2C-⊥	✓	✓	✓			
3	2	4	3A-	✓	✓	✓		✓	✓
			3B-	✓	✓		✓		
			3C-⊥	✓	✓	✓			
4	4	3	4A-	✓	✓	✓			
			4B-	✓	✓		✓	✓	✓
			4C-⊥	✓	✓	✓			
5	7	3	5A-	✓	✓	✓		✓	✓
			5B-	✓	✓		✓		
			5C-⊥	✓	✓	✓			
6	2	3	6A-	✓	✓	✓			
			6B-	✓	✓		✓	✓	✓
			6C-⊥	✓	✓	✓			
7	2	1	7A-	✓	✓	✓			
			7B-	✓	✓		✓		
			7C-⊥	✓	✓	✓			
8	1	5	8A-	✓	✓	✓		✓	✓
9	3	5	9A-	✓	✓	✓		✓	✓
			9B-	✓	✓		✓		
			9C-⊥	✓	✓	✓			

Table 1-1. (Concluded)

Core ID	Test Chamber	Hole #	Test Plug ID ¹	Physical Properties	Ultrasonic velocities	Unconfined compression	Uniaxial Strain	XRD	Thin Section
10	3	4	10A-	✓	✓	✓			
			10B-	✓	✓		✓		
			10C-⊥	✓	✓	✓			
11	2	3	11A-	✓	✓				
			11B-	✓	✓				
			11C-⊥	✓	✓				
12	Left-Hand Drift	1	12A-	✓	✓	✓			
			12B-	✓	✓			✓	✓
			12C-⊥	✓	✓	✓			
13	Left-Hand Drift	1	13A-	✓	✓	✓			
			13B-	✓	✓		✓		
			13C-⊥	✓	✓	✓			

¹ || and ⊥ designations indicate sample orientation with respect to the whole core axis (parallel and perpendicular orientation)

SECTION 2

CORE RECEIPT AND PREPARATION

One cardboard box containing thirteen core sections was delivered to TerraTek on May 9, 1994. Two of the thirteen core sections were broken in two pieces. The remaining core sections were intact with lengths ranging from 50 to 180 mm. All of the core was NX-size and was unpreserved. As outlined in Table 1-1, three sets of test specimens (plugs) were used for characterization testing to examine any anisotropic behavior. Two sets were prepared parallel with respect to the core axis. These samples will be designated as "parallel" (orientation). The other set was prepared orthogonal to the first two sets (perpendicular to the core axis). These test plugs will be referred to as "perpendicular" (orientation). Due to the limited amount of core available only one parallel sample was prepared from core sample #8.

Each test plug was cored from NX whole core using water as the circulating fluid. These test specimens had nominal diameters of 25 mm and lengths of 50 mm for the parallel oriented samples and 38 to 45-mm lengths for the perpendicular oriented samples. The shorter lengths for the perpendicular samples were due to the size restrictions of the NX core. The ends of each specimen were machined flat and parallel to ± 0.025 mm.

The XRD/Lithology samples were selected on the basis of an obvious change in composition or texture. These samples (core numbers 1, 3, 4, 5, 6, 8, 9, and 12) were taken from the excess material surrounding the parallel test plug. One half of the excess material was used for determination of XRD semi-quantitative mineralogy and the other half was cut into a thin section for petrographic examination.

SECTION 3

RESULTS

3.1 XRD MINERALOGY AND LITHOLOGY.

The XRD mineralogy for the eight selected core samples is presented in Table 3-1. The mineralogy in Table 3-1 is semi-quantitative and is reported in percent by mass. The mineralogy is profiled in Figure 3-1 as a function of core sample number. Photomicrographs, illustrating the sample fabric and composition are presented in Appendix B. Specific test procedures used for determining XRD mineralogy are provided in Appendix C.

Table 3-1. Summary of XRD Mineralogy of Selected Samples from the Linchburg Mine

Sample ID	Test Plug ID	Mineralogy, Approximate % by Mass						
		Quartz	Calcite	Serpentine	Talc	Chlorite	Mica \pm Illite ²	Smectite
#1 Ch.4 Hole 2	1A-	1	99					
#3 Ch.2 Hole 4	3A-	20	79					1?
#4 Ch.4 Hole 3	4B-	2	98					
#5 Ch.7 Hole 3	5A-	22		53 ¹	14	2?	9	
#6 Ch.2 Hole 3	6B-	1	99					
#8 Ch.1 Hole 5	8A-	75	25					
#9 Ch.3 Hole 5	9A-	20	80					
#12 L.H. Drift Hole 1	12B-	32	68					

¹ The serpentine group is probably berthierine $((Fe, Al)_3(Si, Al)_2O_5(OH)_4)$.

² X-ray diffraction signature is similar for illite and micaeous minerals. Hence these mineral phases are not differentiated.

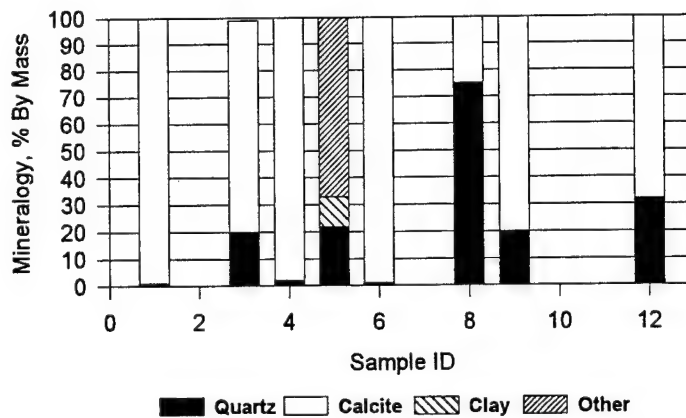


Figure 3-1. XRD mineralogy profile for selected Linchburg Mine samples

3.2 PHYSICAL PROPERTY RESULTS.

Dry bulk density, effective grain density, true grain density, and the derived effective and total porosity for the thirteen core samples are presented in Tables 3-2 and 3-3. Also included in Tables 3-2 and 3-3 are the estimated occluded porosity, as determined from the difference between the total and effective porosity. The procedures used to measure physical properties are presented in Appendix C.

3.3 MECHANICAL PROPERTIES.

Tables 3-4 through 3-8 present the ultrasonic velocities, dynamic properties, compressive strengths, and quasi-static properties determined from unconfined compression and uniaxial strain tests performed on parallel and perpendicular test specimens. Also included in Tables 3-4 and 3-5 is the pre-test bulk density. This was used with the ultrasonic velocities for determination of the dynamic mechanical properties. Table 3-6 reports mechanical properties as well as the pre-test bulk density and effective porosity determined for each test specimen prior to unconfined compression testing. Plots of stress difference versus axial and radial strain (if applicable) are included in Appendix D for the parallel and perpendicular samples tested. Eleven parallel oriented samples were prepared for uniaxial strain testing. Uniaxial strain plots

representing stress difference versus confining pressure, mean normal stress versus volumetric strain, axial stress versus axial strain, and stress difference versus strain difference are provided in Appendix E. Test procedures for the ultrasonic velocity measurements, unconfined compression tests, and uniaxial strain tests are provided in Appendix C.

Table 3-2. Summary of Physical of Material from the Lynchburg Mine

Sample ID	Bulk Density (Mg/m ³)	Effective Grain Density (Mg/m ³)	True Grain Density (Mg/m ³)	Effective Porosity (%)	Total Porosity ¹ (%)	Estimated Occluded Voids (%)
#1A	2.695	2.695	2.700	0.01	0.19	0.18
#1B	2.693	2.693	2.693	0.07	0.07	0.00
#1C ⊥	2.695	2.699	2.708	0.15	0.48	0.33
#2A	2.679	2.702	2.702	0.85	0.85	0.00
#2B	2.674	2.702	2.702	1.04	1.04	0.00
#2C ⊥	2.668	2.695	2.704	1.03	1.33	0.30
#3A	2.645	2.663	2.663	0.66	0.66	0.00
#3B	2.645	2.670	2.670	0.93	0.93	0.00
#3C ⊥	2.641	2.653	2.653	0.44	0.44	0.00
#4A	2.686	2.707	2.707	0.78	0.78	0.00
#4B	2.685	2.725	2.725	1.48	1.48	0.00
#4C ⊥	2.687	2.730	2.730	1.58	1.58	0.00
#5A	2.831	2.835	2.867	0.15	1.26	1.11
#5B	2.831	2.854	2.873	0.82	1.46	0.64
#5C ⊥	2.811	2.820	2.842	0.30	1.09	0.79
#6A	2.691	2.693	2.693	0.08	0.08	0.00
#6B	2.692	2.697	2.697	0.19	0.19	0.00
#6C ⊥	2.690	2.695	2.695	0.20	0.20	0.00

¹ Effective porosity calculated from the bulk volume and grain volume measurements.

Table 3-3. Summary of Physical of Material from the Linchburg Mine

Sample ID	Bulk Density (Mg/m ³)	Effective Grain Density (Mg/m ³)	True Grain Density (Mg/m ³)	Effective Porosity (%)	Total Porosity ¹ (%)	Estimated Occluded Voids (%)
#7A	2.688	2.694	2.694	0.22	0.22	0
#7B	2.686	2.695	2.695	0.33	0.33	0
#7C ⊥	2.684	2.694	2.700	0.36	0.59	0.23
#8A	2.641	2.645	2.649	0.15	0.30	0.15
#9A	2.686	2.699	2.699	0.49	0.49	0
#9B	2.682	2.697	2.701	0.58	0.70	0.12
#9C ⊥	2.689	2.699	2.699	0.36	0.36	0
#10A	2.699	2.703	2.703	0.14	0.14	0
#10B	2.698	2.704	2.704	0.23	0.23	0
#10C ⊥	2.699	2.701	2.701	0.08	0.08	0
#11A	2.648	2.651	2.651	0.09	0.09	0
#11B	2.683	2.691	2.691	0.31	0.31	0
#11C ⊥	2.641	2.672	2.672	1.17	1.17	0
#12A	2.690	2.695	2.695	0.22	0.22	0
#12B	2.627	2.644	2.650	0.65	0.87	0.22
#12C ⊥	2.679	2.691	2.691	0.43	0.43	0
#13A	2.695	2.695	2.699	0.02	0.15	0.13
#13B	2.688	2.697	2.697	0.34	0.34	0
#13C ⊥	2.689	2.697	2.697	0.27	0.27	0

¹ Effective porosity calculated from the bulk volume and grain volume measurements.

Table 3-4. Summary of Ultrasonic Velocities and Dynamic Mechanical Properties

Sample ID	Length (mm)	Bulk Density (Mg/m ³)	P-Wave Velocity (km/s)	S-Wave Velocity (km/s)	Dynamic Poisson's Ratio	Dynamic Moduli		
						Young's (Gpa)	Bulk (Gpa)	Shear (Gpa)
#1A	49.17	2.695	5.31	3.14	0.23	65.4	40.4	26.6
#1B	48.31	2.693	5.48	3.17	0.25	67.5	45.0	27.0
#1C ⊥	43.13	2.695	5.10	3.08	0.21	62.0	35.6	25.6
#2A	36.07	2.679	5.35	2.92	0.29	58.8	46.7	22.8
#2B	50.72	2.674	5.22	3.01	0.25	60.6	40.6	24.2
#2C ⊥	43.89	2.668	5.22	3.09	0.23	62.6	38.7	25.5
#3A	47.93	2.645	5.70	3.58	0.17	79.6	40.2	34.0
#3B	50.72	2.645	5.51	3.72	0.08	79.1	31.4	36.6
#3C ⊥	42.62	2.641	5.49	3.69	0.09	78.2	31.8	35.9
#4A	50.72	2.686	5.31	2.99	0.27	60.9	44.1	24.0
#4B	51.00	2.685	5.60	3.32	0.23	72.7	44.9	29.6
#4C ⊥	43.15	2.687	5.13	2.91	0.26	57.4	39.9	22.8
#5A	45.52	2.831	4.86	3.13	0.15	63.5	30.2	27.6
#5B	41.45	2.831	4.93	3.10	0.17	63.8	32.2	27.3
#5C ⊥	33.83	2.811	5.68	3.52	0.19	82.7	44.5	34.8
#6A	50.95	2.691	5.27	3.07	0.24	63.0	40.4	25.4
#6B	50.95	2.692	5.14	3.05	0.23	61.5	38.0	25.0
#6C ⊥	43.13	2.690	5.13	3.09	0.22	62.4	37.1	25.6

Table 3-5. Summary of Ultrasonic Velocities and Dynamic Mechanical Properties

Sample ID	Length (mm)	Bulk Density (Mg/m ³)	P-Wave Velocity (km/s)	S-Wave Velocity (km/s)	Dynamic Poisson's Ratio	Dynamic Moduli		
						Young's (Gpa)	Bulk (Gpa)	Shear (Gpa)
#7A	50.70	2.688	5.25	2.74	0.31	53.0	46.5	20.2
#7B	51.13	2.686	5.21	2.77	0.30	53.7	44.7	20.6
#7C ⊥	42.60	2.684	5.13	2.79	0.29	53.9	42.8	20.9
#8A	50.24	2.721	5.64	3.78	0.09	84.9	34.5	38.9
#9A	50.60	2.686	5.24	3.04	0.25	61.8	41.2	24.7
#9B	51.13	2.682	5.11	2.95	0.25	58.3	38.9	23.3
#9C ⊥	43.13	2.689	5.22	3.01	0.25	60.9	40.6	24.4
#10A	50.62	2.699	6.09	3.32	0.29	76.6	60.8	29.7
#10B	51.13	2.698	6.04	3.31	0.29	75.9	60.3	29.4
#10C ⊥	42.60	2.699	5.87	3.34	0.26	75.9	52.7	30.1
#11A	51.13	2.648	5.46	3.37	0.19	71.7	38.5	30.1
#11B	50.62	2.683	5.03	2.83	0.27	54.5	39.5	21.5
#11C ⊥	42.62	2.641	5.35	3.33	0.18	69.3	36.1	29.4
#12A	45.77	2.690	5.64	3.21	0.15	69.9	33.3	30.4
#12B	26.82	2.627	5.15	3.53	0.06	69.2	26.2	32.6
#12C ⊥	43.13	2.679	5.94	3.23	0.29	72.1	57.2	27.9
#13A	50.60	2.695	5.74	3.17	0.31	69.3	60.8	26.5
#13B	51.13	2.688	5.71	3.19	0.27	69.6	50.4	27.4
#13C ⊥	42.60	2.689	5.13	3.24	0.17	65.9	33.3	28.2

Table 3-6. Unconfined Compressive Strength and Static Moduli of Samples from
Lynchburg Mine

Sample ID	Bulk Density (Mg/m ³)	Effective Porosity (%)	Compressive Strength (Mpa)	Poisson's Ratio	Static Moduli		
					Young's (Gpa)	Bulk (Gpa)	Shear (Gpa)
#1A	2.695	0.01	95.1	0.24	56.8	36.6	22.9
#1C⊥	2.695	0.15	93.4	0.24	48.0	31.2	19.3
#2B	2.674	1.04	72.5	0.27	57.0	40.6	22.5
#2C⊥	2.668	1.03	89.5	0.27	54.6	40.0	21.4
#3A	2.645	0.66	100.8	0.15	63.1	30.1	27.4
#3C⊥	2.641	0.44	195.5	0.12	70.6	30.8	31.6
#4A	2.686	0.78	83.8	0.25	51.5	35.0	20.5
#4C⊥	2.687	1.58	94.5	0.24	51.2	33.2	20.6
#5A	2.831	0.15	56.0	0.21	42.0	23.8	17.4
#5C⊥	2.811	0.30	58.8	0.39	30.0	47.3	10.8
#6A	2.691	0.08	100.3	0.26	53.2	36.5	21.2
#6C⊥	2.690	0.20	117.3	0.21	49.6	28.6	20.5
#7A	2.688	0.22	85.6	0.22	53.2	31.5	21.9
#7C⊥	2.684	0.36	84.3	0.22	37.6	22.7	15.3
#8A	2.721	0.31	161.6	0.14	72.7	33.6	31.9
#9A	2.686	0.49	107.7	0.25	55.3	36.1	22.2
#9C⊥	2.689	0.36	120.9	0.25	56.6	37.8	22.6
#10A	2.699	0.14	153.9	0.25	62.5	42.3	24.9
#10C⊥	2.699	0.08	177.7	0.31	72.0	63.2	27.5
#11A	2.648	0.09	53.6	0.44	30.3	83.2	10.5
#11C⊥	2.641	1.17	87.4	0.16	60.5	29.3	26.2
#12A	2.690	0.22	116.8	0.25	56.2	37.5	22.5
#12C⊥	2.679	0.43	88.4	0.38	60.9	82.5	22.9
#13A	2.695	0.02	123.3	0.25	61.6	40.5	24.7
#13C⊥	2.689	0.27	70.5	0.26	43.5	30.0	17.3

Table 3-7. Summary of Strength Characteristics Determined from Uniaxial Strain Tests

Sample ID	Maximum Axial Stress Difference (MPa)	Axial Stress Difference Intercept (MPa)	Maximum Volumetric Strain (%)	Measured Permanent Compaction (%)	Confining Pressure at zero Axial Stress Difference (MPa)
#1B	228.6	192.5	1.2	<0.1	180
#2A ¹	170.8	--	0.5	--	200
#3B	284.1	--	0.5	--	--
#4B	204.3	179.7	1.0	0	210
#5B	465.3	226.0	2.1	0.2	77
#6B	251.6	212.8	1.2	<0.1	170
#7B	232.5	197.2	1.4	0.1	273
#9B	239.0	202.1	1.1	0	154
#10B	291.4	249.8	1.0	0	127
#11B ¹	212.5	154.9	0.8	--	--
#13B	256.3	218.7	1.3	0	173

¹ Sample failed (developed a catastrophic shear plane) during uniaxial strain loading. Hence properties were determined (if possible) up to peak axial stress difference.

Table 3-8. Summary of Moduli Determined from Uniaxial Strain Tests

Sample ID	Loading Bulk Modulus (GPa)	Unloading Bulk Modulus (GPa)	Loading Apparent Constrained Modulus (GPa)	Unloading Apparent Constrained Modulus (GPa)	Loading Shear Modulus (GPa)	Unloading Shear Modulus (GPa)
#1B	43.4	50.3	56.1	72.4	6.0	41.3
#2A ¹	38.7	--	59.8	--	--	--
#3B	28.5	--	62.6	--	--	--
#4B	51.0	57.1	67.2	81.1	9.0	53.6
#5B	29.0	36.3	46.3	61.4	19.6	45.6
#6B	44.8	53.6	58.1	78.7	9.5	48.2
#7B	39.6	42.9	49.6	70.3	5.5	57.3
#9B	47.5	56.3	59.4	80.1	9.1	45.6
#10B	55.0	60.1	71.0	88.2	12.4	51.5
#11B ¹	37.7	--	54.9	--	--	--
#13B	41.7	51.9	51.4	76.6	6.6	47.1

¹ Sample failed (developed a catastrophic shear plane) during uniaxial strain loading. Hence, properties were determined (if possible) up to the peak axial stress difference.

SECTION 4

DISCUSSION

4.1 MINERALOGY AND LITHOLOGY.

As is evident in Table 3-1, the Linchburg Mine samples are composed predominantly of calcite and quartz. Core sample #5 is unique in that it contains no calcite and has high amounts of serpentine and talc. Excluding sample #5, the samples contain exclusively calcite and quartz in various proportions. Three distinct mineralogical groups are evident for the samples analyzed. Sample numbers 1, 4, and 6 contain over 90% calcite with minor amounts of quartz. Samples numbers 3, 9, and 12 contain between 68 and 80% calcite and moderate amounts of quartz (20 to 32%). Sample 8 is composed dominantly of quartz (75%) with moderate amounts of calcite (25%).

Several textural features are depicted from thin section photomicrographs (see Appendix B). In general, sample numbers 1, 4, and 6 are medium to coarse-grained crinoidal limestones (packstones/grainstones). Crinoidal fragments appear to dominate the carbonate grains; however, other fossil debris such as bryozoan, bivalve, and coral fragments were observed. Calcitic overgrowth cements these grains and has filled essentially all available pore space. Samples 8 and 12 are fossiliferous chert and samples 3 and 9 are fossiliferous limestone with localized chert zones. For both of these groups, microcrystalline quartz has replaced calcitic fossils to some extent. Fractures are common in these samples (numbers 3, 8, 9, and 12) and are typically filled with calcite. Sample #5 exhibits distinct laminations with alternating thin beds (<1mm) of mudstone, siltstone, and very fine-grained sandstone. The limited porosity occurring in the silty/sandy mudstone is most likely associated with clays.

4.2 PHYSICAL PROPERTIES.

The bulk densities determined for the parallel samples on an average basis are fairly similar, with values ranging from 2.627 to 2.831 Mg/m³ and average approximately 2.690 Mg/m³ \pm 0.005 Mg/m³. The bulk densities determined for the perpendicular samples ranged from 2.641 to 2.811 Mg/m³ and average approximately 2.689 Mg/m³ \pm 0.04 Mg/m³. The highest bulk densities were determined for the laminated silty/sandy mudstone (core #5).

These values reflect the higher concentration of high density iron-magnesium minerals (serpentine, talc, and chlorite) occurring in core #5. The similar values and trends for both the parallel and perpendicular orientation are illustrated in Figure 4-1. The material shows little anisotropy as shown by the random variation between the two orientations. This is substantiated by the extremely small bulk density differences as indicated by the similar average values of 2.690 and 2.689 Mg/m^3 and the small standard deviation for both the parallel and perpendicular samples.

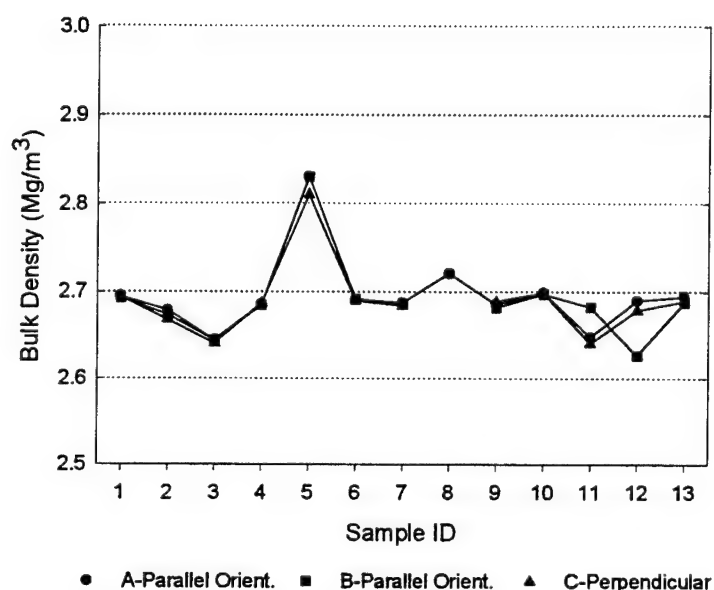


Figure 4-1. Dry bulk density comparison of samples from the Linchburg Mine.

Only minute differences (if any) occur between the effective and "true" grain densities determined for both parallel and perpendicular samples. The average values are 2.702 and 2.704 Mg/m^3 for effective grain densities and 2.705 and 2.708 Mg/m^3 for true grain densities (standard deviations range from ± 0.04 to $\pm 0.05 \text{ Mg/m}^3$). The grain densities ranged from 2.644 to 2.873 Mg/m^3 . Excluding core sample #5, the higher grain densities correlate well with a higher calcite content determined from XRD. Conversely, samples with a higher quartz content have lower grain densities. For example, core sample #8 had a quartz content of 75%, resulting in a relatively lower grain density (2.649 Mg/m^3). Slight differences in grain density may also be attributed to inhomogeneity (preferential sampling of sedimentary structure)

caused by the sample orientation. The parallel samples can contain a number of laminations or "microstrata" (due to the orientation of the whole core with respect to the rock medium), which may be heterogeneous; whereas, the perpendicular samples are oriented along bedding and can contain a limited number of similar laminations or "microstrata". For example, if a core is interbedded with alternating calcite and quartz-rich layers, a perpendicular sample may be dominated by one or the other. In this scenario, the difference could be either 2.70 Mg/m^3 for calcite or 2.65 Mg/m^3 for quartz. A parallel sample will contain several layers depending on their thickness. As a result, the parallel sample will fall between 2.70 and 2.65 Mg/m^3 . Hence, the slight differences between the two orientations may be attributed to localized mineralogical changes and not necessarily anisotropy.

As expected for dense carbonate rocks, porosity is very low. The parallel samples have effective porosities ranging from 0.01 to 1.48%, with an average value of 0.4%. The "total" porosity for the parallel samples is slightly higher with an average value of 0.54%. A somewhat higher porosity was determined for the perpendicular samples. The effective values range from 0.08 to 1.58% and average 0.51%. The total porosity averages approximately 0.67%. The occluded voids for both orientations range from 0 to 1.11% with an average of 0.11%.

Higher porosities were measured for core sample #5, regardless of sample orientation. Also, all of the total porosities were substantially higher than the effective porosities for core #5. This increase in porosity is reflected in the relatively higher occluded void content with values of 1.11%, 0.64%, and 0.79%. This sample was lithologically unique from the other samples due to the lack of carbonates and the occurrence of serpentine, talc, and chlorite. As indicated in Figure 4-2, reasonably consistent values of porosity were measured for the majority of the test samples.

4.3 ULTRASONIC VELOCITIES.

Ultrasonic velocities for both parallel and perpendicular specimens are illustrated in Figures 4-3 and 4-4. The P-wave and S-wave values are very consistent and there is typically little variation with orientation. The P-wave velocities measured on the parallel samples range from 4.86 to 6.09 km/s with an average of $5.40 \text{ km/s} \pm 0.31 \text{ km/s}$. Similar P-wave velocities

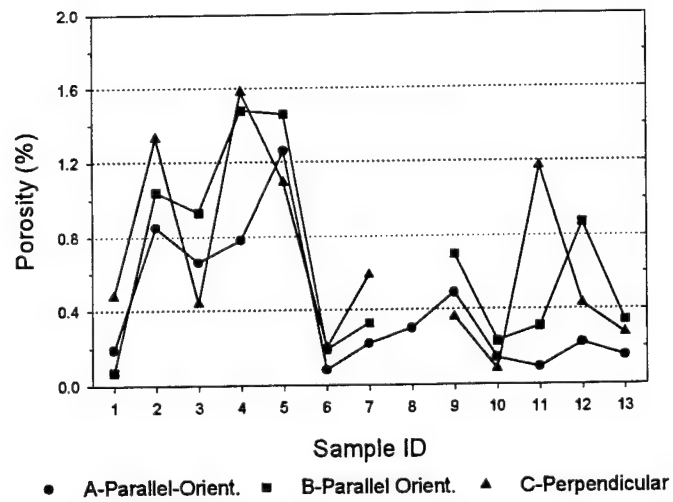


Figure 4-2. Porosity comparison for samples from the Lynchburg Mine.

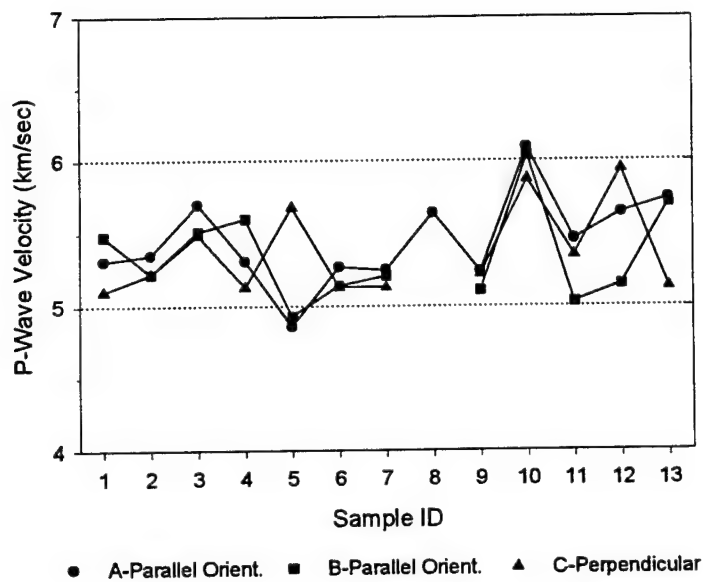


Figure 4-3. P-wave velocities for material from the Lynchburg Mine.

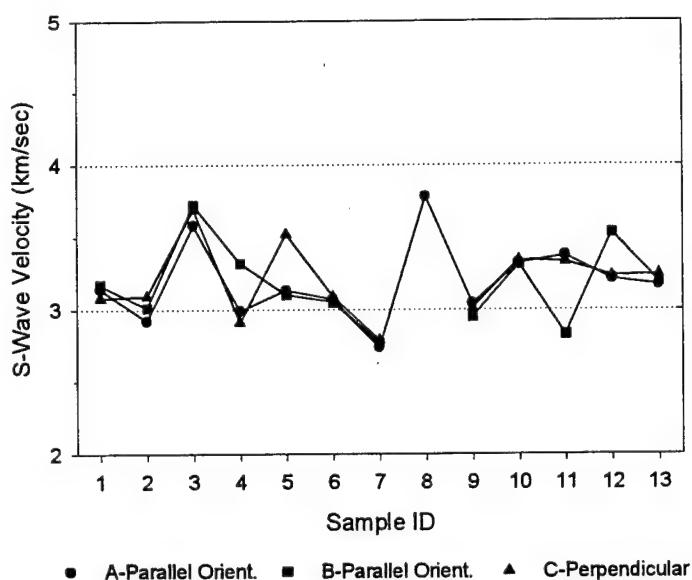


Figure 4-4. S-wave velocities for material from the Linchburg Mine.

measured were determined for the perpendicular samples, which ranged from 5.10 to 5.94 km/s with an average of $5.37 \text{ km/s} \pm 0.31 \text{ km/s}$. The parallel samples from core sample #5 had slightly lower velocities. The slightly lower values determined on the parallel samples from core #5 may be attributed to the direction of the wave front with respect to the orientation of the laminations. In this case, the compressional waves traveled normal to the laminations, resulting in a slower wave velocity. Furthermore, microfractures caused by laminae separations could also have led to a lower compressional wave velocity since these microfractures would be preferentially oriented perpendicular to the wave path. Conversely, the compressional wave travels along the laminations in the perpendicular samples. Hence, when laminations and bedding are present in the sample, a reduction in P-wave velocity is expected for orientations normal to the wave path. The silty/sandy mudstone (core #5) was the only sample exhibiting obvious laminations. The remaining test samples generally appeared massive, exhibiting healed joints and fractures at several orientations. As a result, the average P-wave velocities for the two orientations are exceptionally similar, with values of 5.40 and 5.37 km/s for the parallel and perpendicular samples, respectively.

Similar trends are shown for the S- wave velocities in Figure 4-4. The S-wave velocity average is virtually the same for both orientations, with a values of 3.18 and 3.19 km/s ± 0.26 km/s, respectively.

Average dynamic Young's modulus and Poisson's ratio are 66.6 GPa (± 8.5) and 0.22 (± 0.07), respectively, for the parallel samples. The dynamic Young's modulus and Poisson's ratio were essentially the same for the perpendicular samples, with average values of 66.9 GPa (± 8.8) and 0.22 (± 0.06), respectively. The dynamic bulk and shear moduli average 42.0 GPa and 27.4 GPa for the parallel samples and 40.9 GPa and 27.6 GPa for the perpendicular samples, respectively.

4.4 UNCONFINED COMPRESSION RESULTS.

Overall, the compressive strengths measured at ambient conditions varied from 53.6 to 161.6 MPa for the parallel samples and varied from 58.5 to 195.5 MPa for the perpendicular samples. Strengths determined for the silty/sandy mudstone (core #5) were low with values of 56.0 and 58.8 Mpa. Other low strengths (e. g ., 1 1A - ||) were most likely attributed to pre-existing fractures. The variation in compressive strength is illustrated in Figure 4-5. In many cases, as indicated in Table 3-6 and Appendix A, strengths below 80 MPa were measured on samples exhibiting some sort of structural defect (pre-existing fractures, healed joints, heterogeneity, etc).

Overall, the compressive strengths are fairly similar for both orientations, with average values of 100.8 MPa (± 32.8 MPa) and 106.6 MPa (± 41.2 MPa) for the parallel and perpendicular samples, respectively. There is a weak trend of slightly higher compressive strengths for the perpendicular samples (for eight of twelve test samples). It should be noted that if structural flaws (healed joints etc .) were avoided during preparation the strengths would be considerably higher for many samples. The averages reported were determined from samples that were randomly prepared (i.e. healed joints were not avoided). Hence, it is anticipated that the averages are probably representative of the strata in the vicinity of the test chambers.

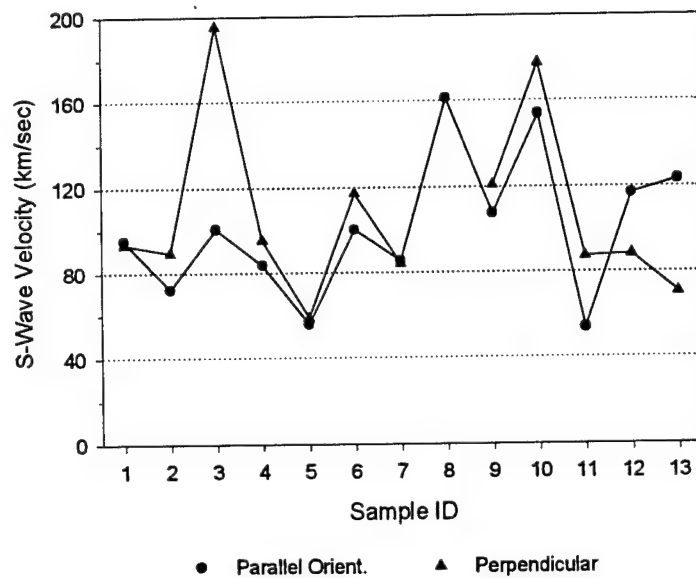


Figure 4-5. Unconfined compressive strengths for material from the Linchburg Mine.

Poisson's ratio determined for the parallel samples averaged 0.24 ± 0.07 , ranging from 0.14 to 0.44. Similar values for Poisson's ratio were determined for the perpendicular samples which range from 0.12 to 0.38 (average of 0.25 ± 0.08).

For the most part, consistent values of Young's modulus were determined for both test sample orientations. Young's modulus for the parallel samples ranges from 30.3 to 72.7 GPa and averages 55.0 GPa (± 10.3 GPa). Young's modulus for the perpendicular samples ranges from 30.0 to 70.6 GPa and averages 52.9 GPa (± 12.4 GPa). Differences in Young's modulus between the two orientations are attributed to fractures, with one exception. The silty/sandy mudstone (core #5) had significant differences in moduli for the two orientations. For this particular rock these differences in moduli are attributed to the orientation of the laminations. The axial load was applied normal to the laminations for the parallel sample. Hence, in this instance, it is easy to visualize more strain due to compacting laminations. Since more strain occurs due to the probable compaction of the laminations, a lower Young's modulus is calculated.

The static bulk and shear moduli showed less variation between orientations, with the parallel samples averaging 39.0 and 22.3 GPa, and the perpendicular samples averaging 39.7 and 21.3 GPa, respectively.

Significant and important differences are seen between the static and dynamic mechanical properties. The dynamic values are predominantly higher than their static counterparts. The dynamic Young's moduli average approximately 1.2 to 1.3 times higher than the static values for the parallel and perpendicular sample sets, respectively.

The differences observed in dynamic versus static properties may be attributed to the degree of elastic versus non-recoverable response of the material tested. The dynamic moduli primarily sense an elastic response to extremely low stresses and strains. The static moduli are based on a more elastic/permanent deformation response to higher stresses and strains. Dynamic moduli over a continuous vertical profile, can theoretically be determined from sonic logging. The ideal scenario is a cross-correlation between static and dynamic laboratory values and logging values. This would allow routine logging procedures to be used (i.e., density and velocity logs), with correlation of the logging values as required.

4.5 UNIAXIAL STRAIN RESULTS.

As indicated in Tables 3-1 and 3-8, eleven uniaxial strain tests were performed on parallel oriented test samples. Test sample 12B was too short for testing and core sample #8 was of insufficient size for more than one test sample. Three of the eleven samples failed during uniaxial strain loading. Test samples 2A, 3B, and 11B were all heterogeneous, exhibiting multiple, pre-existing fractures. These pre-existing sample conditions contributed to sample failure during uniaxial strain loading.

The maximum axial stress difference reached during uniaxial strain loading ranged from 170.8 to 465.3 Mpa. Permanent compaction following uniaxial strain and hydrostatic unloading ranged from 0 to 0.2%. Higher values of permanent compaction correlates with higher values of axial stress difference. The maximum volumetric strain measured ranged from 0.5 to 2.1% (maximum volumetric strain typically occurs at the maximum mean normal stress during uniaxial strain loading).

Bulk, apparent constrained, and shear moduli were determined from both the loading and unloading stress-strain curves. For dense material, such as the material from the Linchburg mine, the loading bulk modulus was determined from between zero and the peak mean normal stress (mean normal stress versus volumetric strain). The unloading bulk modulus was determined from the peak mean normal stress to a mean normal stress level where hydrostatic unloading began. The loading and unloading apparent constrained modulus were calculated from the axial stress versus axial strain curves. For both the loading and unloading segments, the slope of the line occurring between approximately 100 MPa and the peak axial stress was used. The loading and unloading shear modulus was determined from the axial stress difference versus the strain difference curves. The loading shear modulus was determined between approximately 50% and the peak axial stress difference, and the unloading shear modulus was calculated between the peak axial stress difference and approximately 50% of the unloading curve.

The loading and unloading bulk moduli ranged from 28.5 to 55.0 GPa and 36.3 to 60.1 GPa, respectively. The loading apparent constrained modulus ranged from 46.3 to 71.0 GPa and the unloading apparent constrained modulus ranged from 61.4 to 88.2 GPa. The loading and unloading shear moduli ranged from 5.5 to 19.6 GPa and 41.3 to 57.3 GPa, respectively.

APPENDIX A
TEST SAMPLE IDENTIFICATION AND INITIAL CONDITION

Core # ID	Test Plug ID	Comments/Initial Condition
#1 Ch. 4 Hole 2	1A-	Dense limestone - minor fractures (healed with probable calcite), fairly homogeneous, coarse grained.
	1B-	Dense limestone - minor fractures (healed with probable calcite), fairly homogeneous, coarse grained.
	1C-⊥	Dense limestone - heterogeneous, 1/3 sample is fine-grained and 2/3 coarse. Healed fracture along contact between fine and coarse grained material.
#2 Ch. 4 Hole 2	2A-	Dense limestone - multiple fractures at various angles (partially healed), fairly homogeneous, coarse grained.
	2B-	Dense limestone - multiple fractures at various angles (partially healed), fairly homogeneous, coarse grained.
	2C-⊥	Dense limestone - fractures oriented sub-parallel to plug axis (partially healed), heterogeneous, coarse grained with chert nodules.
#3 Ch. 2 Hole 4	3A-	Partially silicified limestone - multiple fractures (healed with calcite?) at various angles, medium to coarse grained, heterogeneous.
	3B-	Partially silicified limestone - multiple fractures (healed with calcite?) at various angles, heterogeneous, fine to coarse grained.
	3C-⊥	Partially silicified limestone - multiple fractures (healed with calcite?) at various angles, heterogeneous, fine to coarse grained.
#4 Ch. 4 Hole 3	4A-	Dense limestone - minor healed fractures at various angles, homogeneous, coarse grained.
	4B-	Dense limestone - minor healed fractures at various angles, homogeneous, coarse grained.
	4C-⊥	Dense limestone - fractures sub-parallel to plug axis (healed with calcite?), homogeneous, coarse grained.
#5 Ch. 7 Hole 3	5A-	Interbedded mudstone - layers of silt, mud, and sand oriented sub-perpendicular to plug axis, heterogeneous, millimeter clasts abundant.
	5B-	Interbedded mudstone - layers of silt, mud, and sand oriented sub-perpendicular to plug axis, heterogeneous, clasts.
	5C-⊥	Interbedded mudstone - layers of silt and mud and sand oriented sub-parallel to plug axis, heterogeneous, minor fractures, clasts.

Core # ID	Test Plug ID	Comments/Initial Condition
#6 Ch. 2 Hole 3	6A-	Dense limestone - minor fractures (healed with probable calcite) sub-parallel to plug axis, homogeneous, medium grained.
	6B-	Dense limestone - minor fractures (healed with probable calcite) sub-parallel to plug axis, homogeneous, medium grained.
	6C-⊥	Dense limestone - minor fractures (healed with probable calcite) at various angles to plug axis, homogeneous, medium grained.
#7 Ch. 2 Hole 1	7A-	Dense limestone - minor fractures at various angles (healed with calcite?), homogeneous, coarse grained.
	7B-	Dense limestone - fractures at various angles (healed with calcite?), heterogeneous, fine to coarse grained.
	7C-⊥	Dense limestone - fractures oriented sub-perpendicular to plug axis (healed with calcite?), heterogeneous, fine to coarse grained.
#8 Ch. 1 Hole 5	8A-	Silicified limestone - fractures at various angles (healed with calcite?), fairly homogeneous, fine to medium grained.
#9 Ch. 3 Hole 5	9A-	Dense limestone - minor fractures at various angles, fairly homogeneous, medium to coarse grained.
	9B-	Dense limestone - fractures at various angles (healed with calcite?), heterogeneous, fine to medium grained with chert nodules.
	9C-⊥	Dense limestone - minor fractures at various angles, homogeneous, fine to medium grained.
#10 Ch. 3 Hole 4	10A-	Dense limestone - minor fractures at various angles, fairly homogeneous with predominantly fine grained material, coarser material consisting of lithic clasts and chert lenses observed.
	10B-	Dense limestone - large fracture at 30° to plug axis (calcite healed), fairly homogeneous with predominantly fine grained material, coarser material (lithic clasts and chert) observed.
	10C-⊥	Dense limestone - minor fractures sub-perpendicular to plug axis, fairly homogeneous, dominantly fine grained with minor amounts of coarse material.

Core # ID	Test Plug ID	Comments/Initial Condition
#11 Ch. 2 Hole 3	11A-	Partially silicified dense limestone - fractures at various angles (partially healed with probable calcite), heterogeneous with fine and coarse grained material.
	11B-	Silicified dense limestone - fractures at various angles (healed with probable calcite), heterogeneous with two distinct layers sub-parallel to plug axis. One layer is silicified and the other is calcareous.
	11C-⊥	Chert - fractures at various angles (partially healed with calcite?), heterogeneous with coarse carbonate clasts and chert nodules.
#12 L.H. Drift Hole 4	12A-	Dense limestone with chert - fractures at various angles (healed with calcite?), heterogeneous with medium grained carbonates and substantial chert clasts.
	12B-	Dense limestone with chert - fractures at various angles (healed with calcite?), heterogeneous, fine to medium grained carbonates and substantial chert clasts (short sample <25mm in length).
	12C-⊥	Dense limestone - fractures at various angles (healed with calcite?), heterogeneous, predominantly fine to medium grained carbonates with minor amounts of chert clasts.
#13 L.H. Drift Hole 1	13C-	Dense limestone - minor fractures at various angles, fairly homogeneous, medium grained with minor amounts of chert clasts.
	13B-	Dense limestone - fractures at various angles (healed with calcite?), fairly homogeneous, medium grained.
	13C-⊥	Dense limestone - fractures sub-perpendicular to plug axis, fairly homogeneous, medium grained.

APPENDIX B
THIN SECTION MICROGRAPHS AND DESCRIPTIONS

PLATE 1

Sample No. 1

- A. Low-magnification overview of medium-to-coarsely crystalline crinoidal limestone. Large, uncrystalline crinoid fragments constitute the most abundant grain type, though less common bryozoan, bivalve, and coral fragments are also present. Grains are well cemented by calcitic, syntaxial overgrowth cement, leaving essentially no interparticle porosity. Crinoid fragments in the lower portion of view exhibit minor replacement by chert (light-brown patches). Plane-polarized light. (20X)
- B. Higher-magnification view of crinoid (and a few bryozoan) fragments and syntaxial overgrowth cement. Original allochems are characterized by a "dirtier" appearance in comparison to "clean", inclusion-free overgrowths. Note that interparticle pores are thoroughly occluded by cement. Linear feature in the right portion of view is a thin, calcite-filled fracture. Plane-polarized light. (40X)

Sample No. 3

- C. General overview of fractured chert illustrating how microcrystalline quartz has replaced what was once fossiliferous limestone (note possible fenestellid bryozoan in the center of view). Cross-cutting fractures are commonly filled with calcite (pink-stained) and finely crystalline, greenish clays. Larger fractures, not shown here, may contain cherty gouge fragments, in addition to cements. Disseminated calcite in the matrix could represent unreplaced original calcite or calcite that has replaced chert during and/or after fracturing. Lack of visible blue epoxy in this view indicates the tight, nonporous nature of the sample fabric. Plane-polarized light. (20X)
- D. Higher-magnification view showing how quartz occurs as microcrystalline (cherty) replacement, pore- and fracture-filling megaquartz, and minor pore-filling chalcedony. Also shown are calcite-filled fractures and unreplaced biotic fragments. Original biotic fragments and other allochems include crinoid debris, bryozoans, bivalve fragments, and possible nonskeletal grains; in most cases, however, they are difficult to identify because of poor preservation of internal structure. Crossed nicols. (40X)



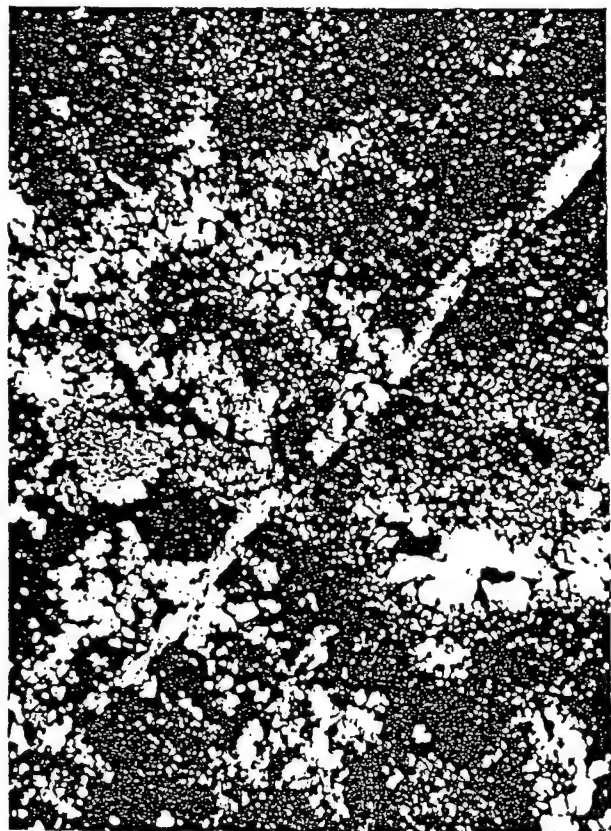
A



B



C



D

PLATE 2

Sample No. 4

- A. General overview of coarsely crystalline, crinoidal limestone. Though crinoids are most pervasive, other grain types include bryozoan and bivalve fragments, and rare Foraminifera. Intense physical and chemical compaction has produced interpenetrative and sutured grain contacts and numerous microstylolites. The primary stylolite in the center of view has juxtaposed areas of differing grain size (lower portion of view is notably finer-grained). White, rounded patches are sites of replacement by chalcedony. Plane-polarized light. (40X)
- B. Detailed view highlighting a crinoid fragment that has been partially replaced by microcrystalline quartz. Compaction of grains was less intense in this portion of the sample because grains are only somewhat flattened and syntaxial overgrowths are intact. Porosity in this sample is limited to thin, partially open microfractures. Crossed nicols. (40X)

Sample No. 5

- C. Low-magnification overview of wavy-to-irregularly laminated, silty/sandy mudstone. Lamination is defined by alternation of thin beds of mudstone, siltstone, and very fine-grained sandstone. Wavy, convoluted texture and lenticular beds are most likely the result of both bioturbation and soft-sediment deformation. Porosity is restricted to microporosity associated with clay matrix and narrow dehydration fractures. Plane-polarized light. (20X)
- D. Higher-magnification view of texture illustrating matrix-supported fabric and grain types. Grains are angular and poorly sorted, and are commonly composed of mono- and polycrystalline quartz, chert, possible glauconite (light-brown grains), shaly rip-up clasts, and accessory pyrite, zircon, and tourmaline. Larger, irregularly shaped grains are biotic fragments partially replaced by chert, illite/mica, and/or pyrite. Clay-rich matrix is most likely composed of mixed-layer illite-smectite. Plane-polarized light. (40X)



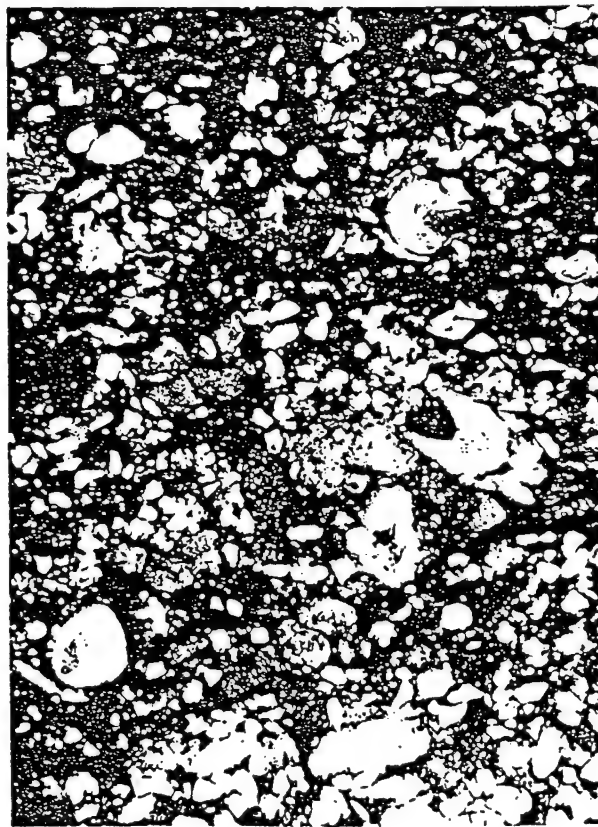
A



B



C



D

PLATE 3

Sample No. 6

- A. Low-magnification overview of medium-to-coarsely crystalline limestone containing abundant crinoid debris and other fossil fragments. Interpenetrative-to-sutured grain contacts, stylolites, and microstylolites record intense grain compaction. Most interparticle calcite cement has been dissolved during chemical compaction and stylolitization. Note the lack of visible porosity in the sample fabric. Plane-polarized light. (20X)
- B. Detailed view of unstained portion of the sample highlighting compaction features. Microstylolites are characterized by high amplitudes and thin residue seams, whereas better developed stylolites exhibit low amplitudes and thick residue seams. Flattened and irregular grain shapes also indicate intense compaction. Single-unit crystals are most likely echinoderms, and foliated or layered fragments are derived from bivalves. Plane-polarized light. (40X)

Sample No. 8

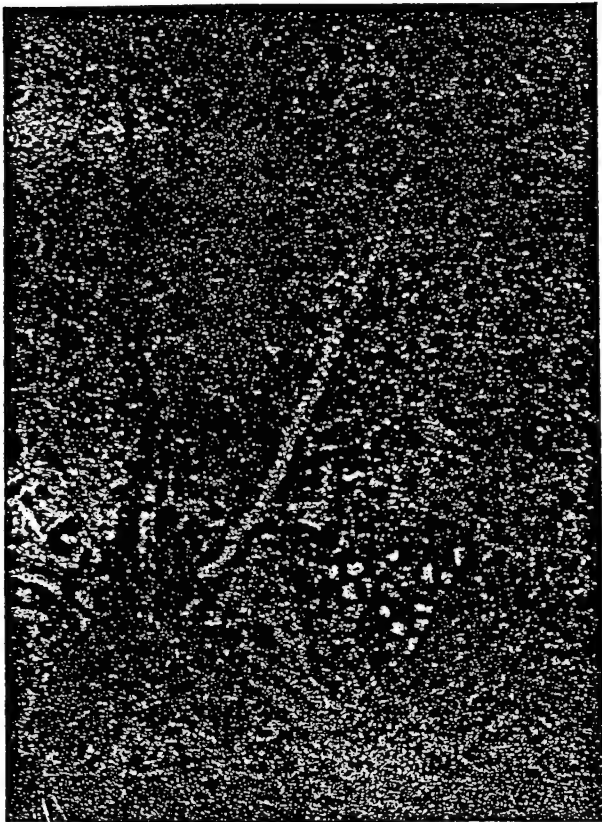
- C. General overview of fossiliferous chert containing relict bryozoan fragments. Texture in this sample is similar to that in sample 3, where microcrystalline and chalcedonic quartz have thoroughly replaced bioclastic limestone. Numerous filled and partially filled natural fractures, three of which are shown here, also characterize this sample. Common fracture fillings include calcite, quartz, and clay. Isolated fracture porosity is the only porosity type visible in this view and throughout the sample. Plane-polarized light. (20X)
- D. Higher-magnification view of pervasive chert replacement. Though most original skeletal fragments have been replaced, some remain calcitic, such as the large echinoderm fragment exhibiting high relief. The distribution of fibrous chalcedony indicates that it is most likely filling or replacing original intergranular pores. Note partially clay-filled fracture cross-cutting fabric in the center of view. Crossed-nicols. (40X)



A



B



C



D

PLATE 4

Sample No. 9

- A. Low-magnification overview of coarsely crystalline, fossiliferous limestone. General texture is similar to that in other limestone samples in this study, but contains more bryozoan debris in addition to crinoids, bivalves, ostracodes, ooids, and intraclasts. Sparry calcite occurs as an interparticle, syntaxial overgrowth cement and eliminates essentially all interparticle pore space. Compaction features are not nearly so well developed in this sample, and replacement by chert is very minor in extent. Plane-polarized light. (20X)
- B. Detailed view of a coated intraclast containing biotic fragments and syntaxial overgrowth cement. Outside of intraclast, grains include crinoids, bryozoans, and bivalves well cemented by "cleaner" calcite spar. The lack of blue epoxy indicates the paucity of visible porosity in this sample. Plane-polarized light. (40X)

Sample No. 12

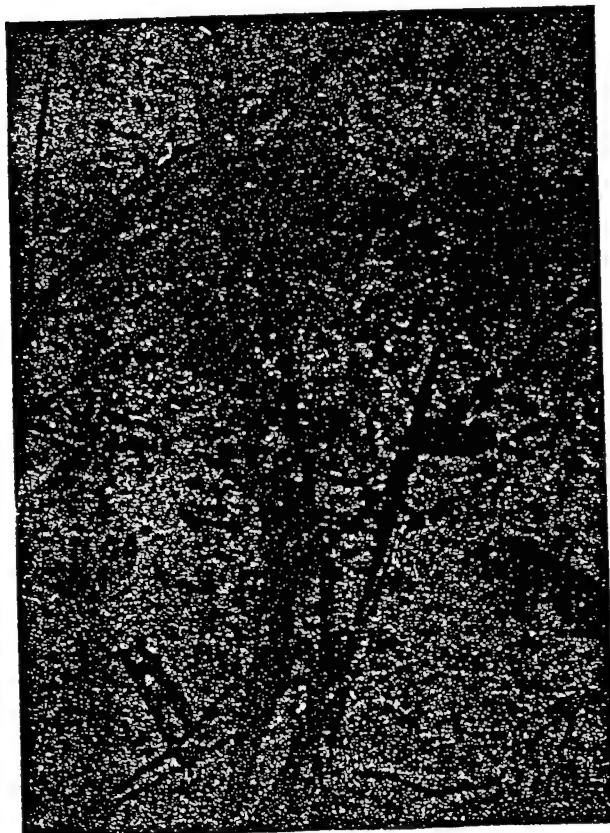
- C. General overview of highly fractured chert exhibiting much of its original limestone texture. Darker patches represent replaced "ghosts" of original fossil fragments, such as crinoids and bryozoans. Parts of this sample have remained calcite and unreplaced by quartz. Nature and orientation of cross-cutting microfractures indicate that several generations of fractures are present. Larger fracture in the center of view contains angular, cherty gouge material cemented by calcite. Narrower fractures exhibit some open porosity (blue). Plane-polarized light. (20X)
- D. High-magnification view of fracture-filling material. Platy-to-fibrous green mineral is interpreted as clay; its fairly high birefringence and greenish-brown color suggest that it is an Fe/Mg-rich muscovite (phengite). Clay most likely precipitated after calcite. Note nearby microfracture and dissolution porosity. Plane-polarized light. (100X)



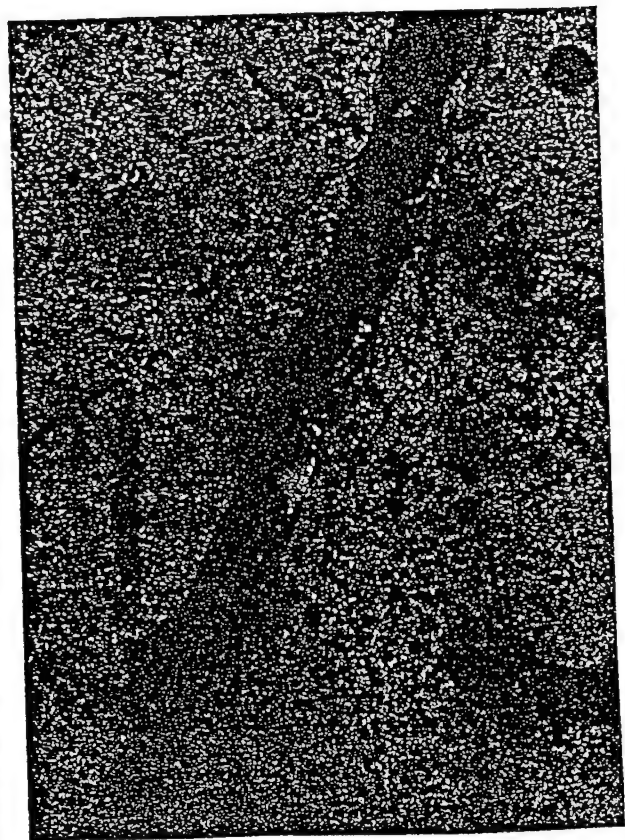
A



B



C



D

APPENDIX C
TEST PROCEDURES

C.1 XRD AND LITHOLOGIC EXAMINATION.

X-Ray Diffraction (XRD) was performed to quantify the mineralogy of the eight of 13 core sections. The analysis was performed on representative 1-g splits of the bulk samples. XRD samples were ground in acetone in an agate mortar to pass a 45- μm sieve. The powder was X-rayed at $2^\circ 2\theta$ per minute from 10 to $65^\circ 2\theta$, and $1^\circ 2\theta$ per minute from 2 to $10^\circ 2\theta$, using a Phillips XRG-3100 diffractometer. Duplicate samples were X-rayed to verify the existence of minerals detected in the original samples. Approximate percentage by mass of individual minerals were determined by comparing diagnostic peak intensities with those generated by standard pure phases, mixed in various known proportions.

Lithologic examination, using hand samples and thin sections, was performed to distinguish textural and compositional variations in the eight samples. The thin sections were stained for calcite identification and were injected with blue epoxy for pore space detection. Photomicrographs were taken to illustrate sample fabric, including porosity, fossil content, and mineralogy. These descriptions were conducted to compliment the measurements of mechanical properties as determined from the ultrasonic velocity present uniaxial compression and uniaxial strain testing. Hence, detailed descriptions characterizing specific fossils and depositional environments, were not performed.

C.2 PHYSICAL PROPERTY MEASUREMENTS.

As part of the initial material characterization, the effective grain density, dry bulk density, and effective porosity were determined. Non-destructive physical property measurements were performed on each test specimen (parallel and perpendicular orientation).

Prior to any testing, each test specimen was oven dried at 105°C for period of 24 hours. Bulk volume was determined using the mercury immersion technique. The bulk density was determined simply by dividing the mass of the test specimen by its bulk volume.

The effective grain volume was determined on each test specimen using the gas pycnometry technique. Gas pycnometry is based on Boyle's Law, which holds that, for a gas at constant temperature, the volume of the gas will vary inversely with the pressure:

$$\frac{P_1}{P_2} = \frac{V_2}{V_1} \quad (\text{C.1})$$

where:

P_1 is the initial pressure in V_1 ,

P_2 is the final pressure in V_2 ,

V_1 is the initial volume, and

V_2 is the final volume.

A calibration curve is constructed by measuring the volume of known, standard billets. The known volumes are plotted against the ratio P_1/P_2 and a linear equation is fitted to the data. The recorded pressure ratio with a sample in the porosimeter is then used to determine the effective grain volume (V_g) from the calibration curve. The grain density is calculated as follows:

$$\rho_g = \frac{W}{V_g} \quad \{C.2\}$$

where:

ρ_g is the grain density,

W is the pre-test mass, and

V_g is the grain volume determined from the porosimeter.

A fabricated gas expansion porosimeter is used at TerraTek, helium gas is used. The grain densities determined with gas pycnometry for intact plug specimens are effective grain densities, not total, as the gases only penetrate interconnected porosity. Hence, porosity derived from the effective grain density is an indication of interconnected porosity, not the true total porosity. In order to measure the specimen's total porosity, a supplementary destructive grain density technique is required.

Grain density was measured again on post-test specimens, also using gas pycnometry. Following the mechanical testing, each test specimen was reduced to a powder capable of passing through a 45- μm sieve. A dried powdered sample (dried at 105°C for 16 to 24 hours), weighing between 25 and 35 g (W_d), is placed into a cup which is inserted into the porosimeter vessel. The volume of the powder is determined as intact plug specimen. This yields true grain density.

Both the effective and the total porosity are calculated using the following relation:

$$\phi = 1 - \frac{\rho_d}{\rho_g} \quad (C.3)$$

where:

ϕ is the porosity (either effective or total),

ρ_d is the dry bulk density, and

ρ_g is the grain density (effective or true).

C.3 ULTRASONIC VELOCITY MEASUREMENTS.

Compressional (P) and shear (S) wave velocities were measured on all test specimens (parallel and perpendicular orientation) at bench conditions; specifically at a nominal axial stress of approximately 1 MPa. To measure the P and S-wave velocities, two piezoelectric 1-MHz crystals were placed in mechanical contact with the sample, one at each end. A high voltage pulse of short duration was then applied to one of the crystals, using a pulse generator. This pulse was received by the crystal at the opposite end of the specimen. Based on the time required for the pulse to travel through length of the specimen, the P and S-wave velocities were calculated. The formula for calculating the dynamic properties are as follows¹:

$$E_D = C_s^2 \rho \left[\frac{3 \left(\frac{C_p}{C_s} \right)^2 + 4}{\left(\frac{C_p}{C_s} \right)^2 + 1} \right] \quad (C.4)$$

¹ Jaeger, J. C. and Cook, N. G. W., *Fundamentals of Rock Mechanics*, Chapman and Hall, pp. 183-187, 1979.

$$V_D = \frac{1}{2} \left[\frac{\left(\frac{C_p}{C_s}\right)^2}{\left(\frac{C_p}{C_s}\right)^2 + 1} \right] \quad (C.5)$$

$$K_D = \rho \left(C_p^2 + \frac{4}{3} C_s^2 \right) \quad (C.6)$$

$$G_D = \frac{C_s^2}{2} (\rho) \quad (C.7)$$

where:

E_D is Young's modulus,

V_D is Poisson's ratio,

K_D is Bulk modulus,

G_D is Shear modulus,

ρ is Bulk density,

C_p is Compressional velocity, and

C_s is Shear velocity.

C.4 UNIAXIAL COMPRESSION TESTS.

After the physical and ultrasonic-velocity measurements were performed, one of the parallel samples and the perpendicular sample were mechanically tested to determine unconfined compressive strength. In addition, elastic moduli were calculated from the measured deformation resulting from the applied axial stress. The Linchburg mine material is dominated by competent

dense limestone. For several samples, it was anticipated that brittle catastrophic failure would ensue on reaching the maximum compressive strength of the material under unconfined conditions (zero confining pressure). Hence, for some samples, two loading cycles were performed to protect the transducers that measure axial and radial deformation. During the first cycle, axial and radial deformation were recorded up to an axial stress of 100 MPa on the first cycle. Prior to the second cycle, the axial stress was reduced to zero and the radial transducers (cantilevers) were removed. The sample was then loaded to failure. In most cases, the test sample unexpectedly failed prior to 100 MPa. Hence, stress-strain data exists to failure for these samples. Axial stress for both loading cycles was increased using a servo-controlled axial strain rate of $1 \times 10^{-5}/s$. Axial strain, radial strain and axial stress were recorded continuously (where applicable) through both loading cycles, using a digital data acquisition system.

C.5 UNIAXIAL STRAIN TESTS.

Uniaxial Strain: An axial compressive stress was applied such that a constant axial strain rate was maintained while the confining pressure was varied to maintain zero radial strain. The load piston was reversed when the confining pressure reached a prescribed value and the sample was unloaded to a hydrostatic stress state while maintaining the zero radial strain condition. The hydrostatic stress was typically unloaded to zero pressure at a nominal rate of 1.4 MPa/s. The loading and unloading constrained modulus, bulk modulus, and shear modulus, and the permanent compaction were typically determined.

Specific parameters were calculated from the uniaxial strain tests. For completeness, some of the more common terms are defined as follows.

Maximum volumetric strain. The maximum volumetric strain occurring during a uniaxial strain test usually occurs at the maximum mean normal stress level (confining pressure of about 400 Mpa). Under uniaxial strain conditions, the volumetric strain is represented by the axial deformation since radial strain is prevented.

Measured permanent compaction (MPC). This is the "permanent" volumetric strain existing after a load -unload cycle following a uniaxial strain test, to a maximum lateral stress of 400 Mpa. This is the non-recoverable deformation following a uniaxial strain test and is directly related to the volume of air-filled voids (void collapse due to shear enhanced compaction) occurring in the sample prior to testing.

Loading bulk modulus. This is the slope of the line on the mean normal stress versus volumetric strain curve from a point on the curve which is vertically above the measured permanent compaction and extending to the maximum mean normal stress. This region of the loading curve is primarily influenced by the intrinsic properties of the solid material (most of the air-filled voids are presumably crushed).

Unloading bulk modulus. This is the slope of the line on the mean normal stress versus volumetric strain curve extending from the maximum mean normal stress to a point at which hydrostatic unloading begins (axial stress difference of zero).

Loading apparent constrained modulus. This is the slope of the line on the axial stress versus axial strain curve extending from a point on the loading curve that occurs vertically above where the axial stress equals zero on the unloading curve to the maximum axial stress.

Unloading apparent constrained modulus. This is the slope of the line on the axial stress versus axial strain curve extending from the maximum axial stress to a point on the unloading curve where hydrostatic unloading begins.

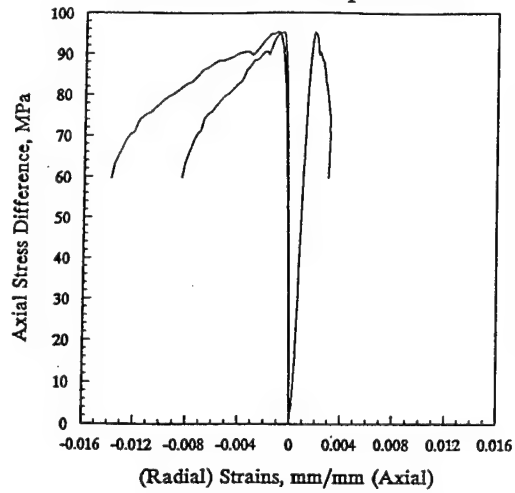
Loading shear modulus. This is the slope of the line on the axial stress difference versus strain difference curve extending from approximately 50% of the measured strain during loading to the maximum stress difference.

Unloading shear modulus. This is the slope of the line on the axial stress difference versus strain difference curve extending from the maximum stress difference to a point in the curve at approximately 50% at the stress difference during unloading curve.

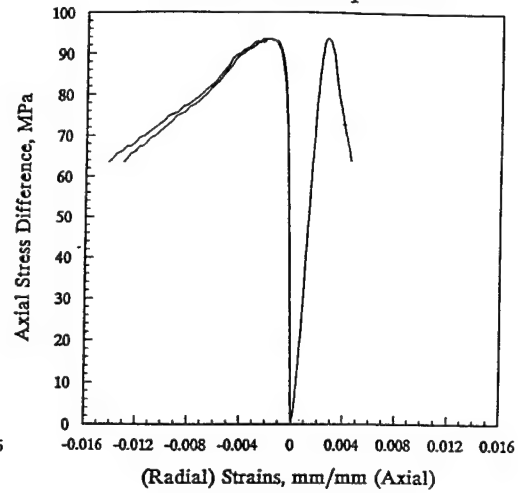
Maximum axial stress difference. This is the maximum stress difference usually occurs at the peak lateral stress (400 MPa) during a uniaxial strain test.

APPENDIX D
STRESS-STRAIN PLOTS
UNCONFINED COMPRESSION TESTS

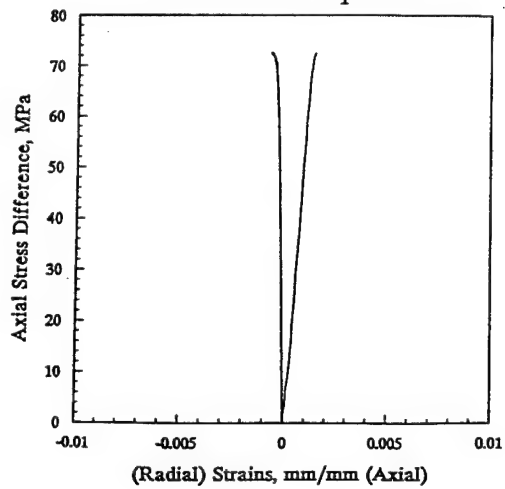
DNA #1A - Parallel
Unconfined Compression



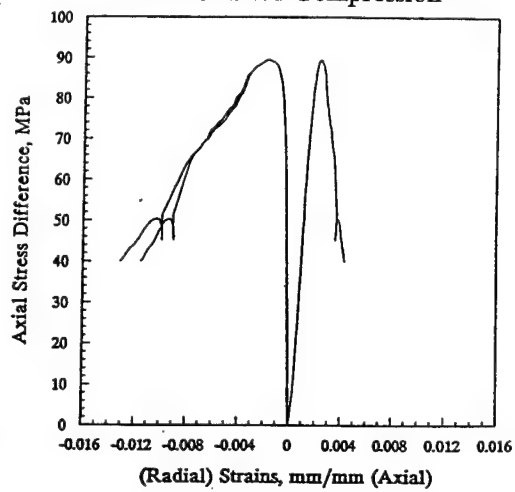
DNA #1C - Perpendicular
Unconfined Compression



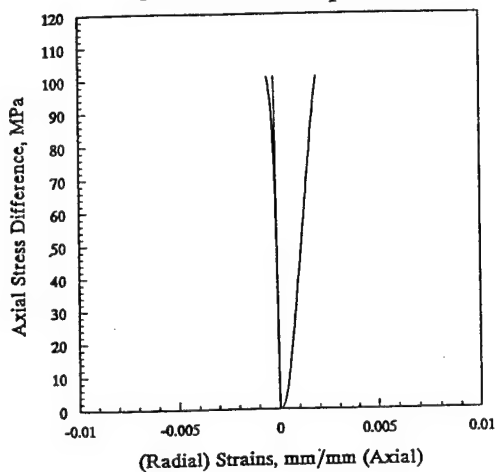
DNA #2B - Parallel
Unconfined Compression



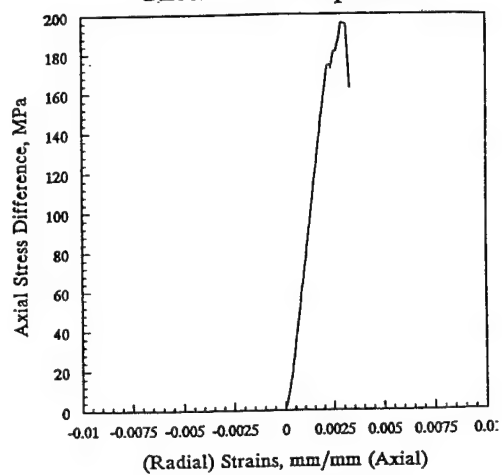
DNA #2C - Perpendicular
Unconfined Compression



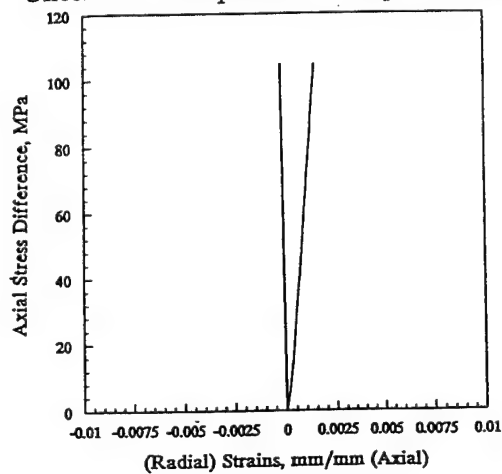
DNA #3A - Parallel
Unconfined Compression



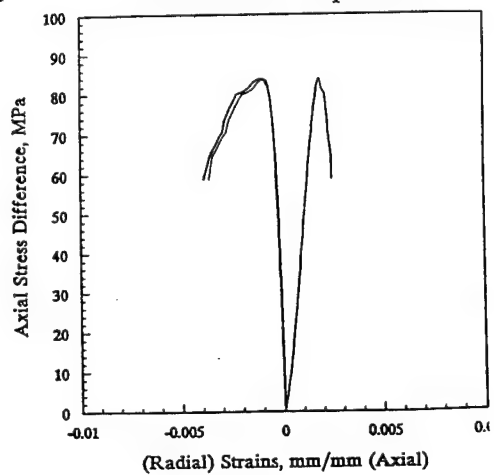
DNA #3C - Perpendicular
Unconfined Compression



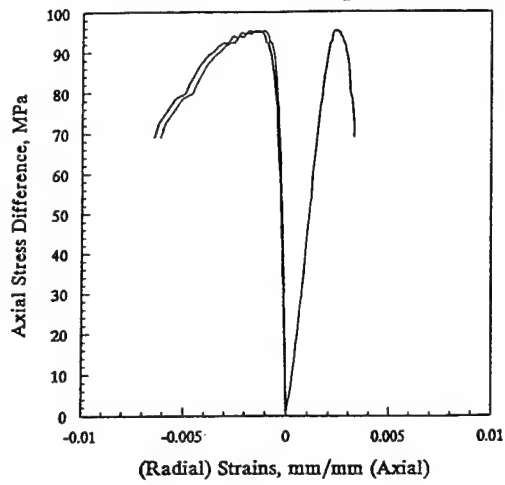
DNA #3C - Perpendicular
Unconfined Compression - Sample not Failed



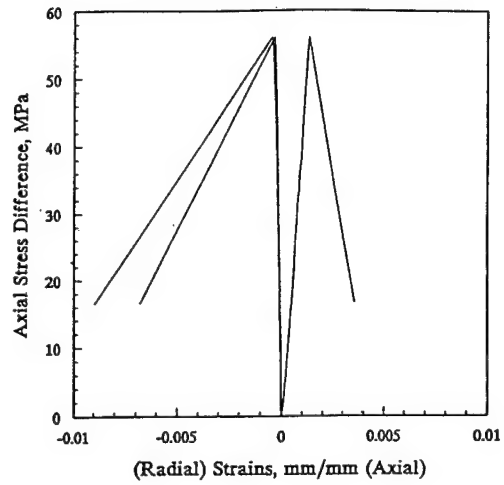
DNA #4A - Parallel
Unconfined Compression



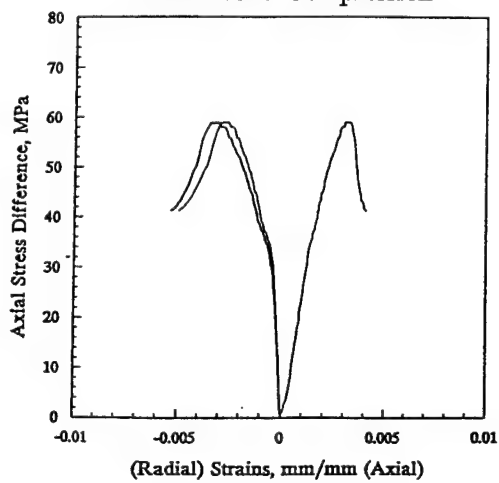
DNA #4C - Perpendicular
Unconfined Compression



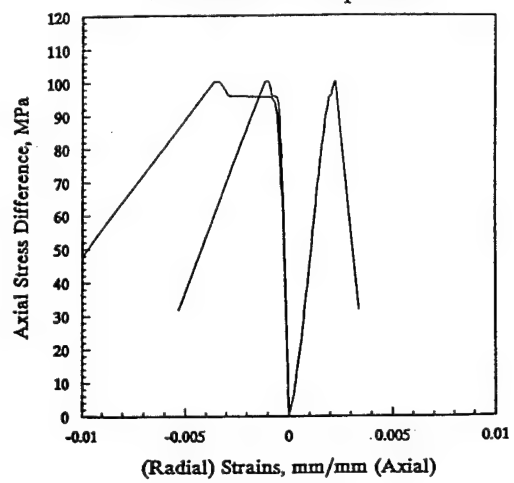
DNA #5A - Parallel
Unconfined Compression



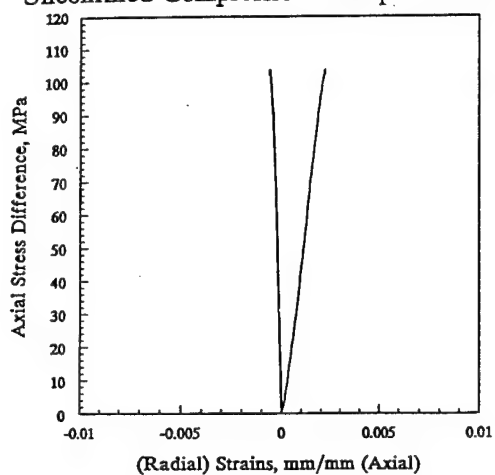
DNA #5C - Perpendicular
Unconfined Compression



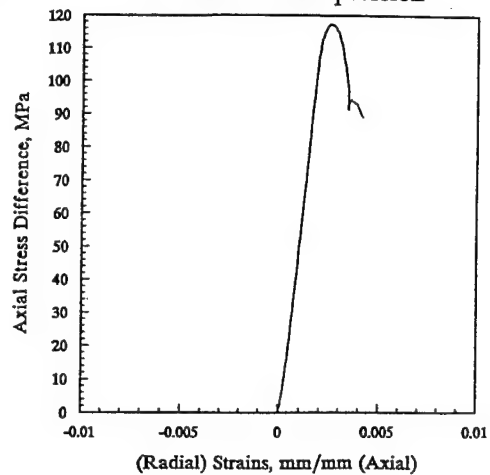
DNA #6A - Parallel
Unconfined Compression



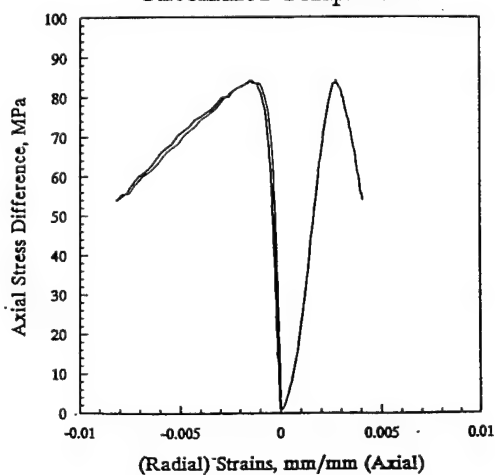
DNA #6C - Perpendicular
Unconfined Compression - Sample Not Failed



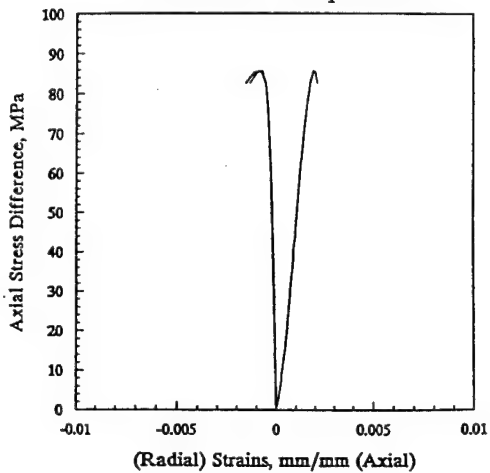
DNA #6C - Perpendicular
Unconfined Compression



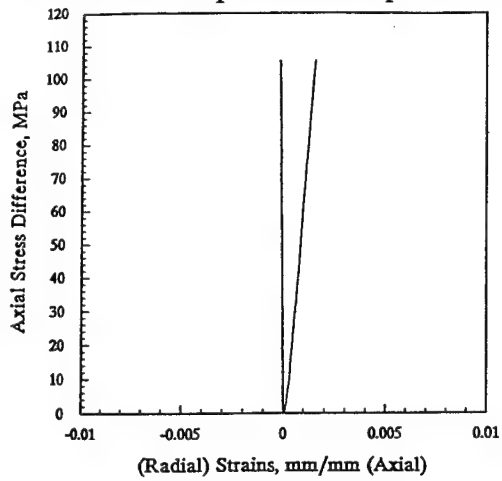
DNA #7C - Perpendicular
Unconfined Compression



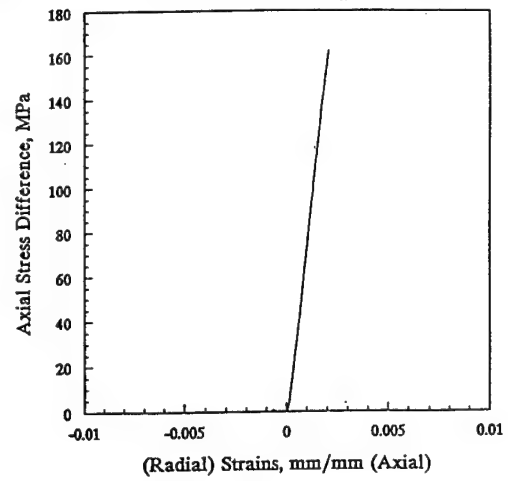
DNA #7A - Parallel
Unconfined Compression



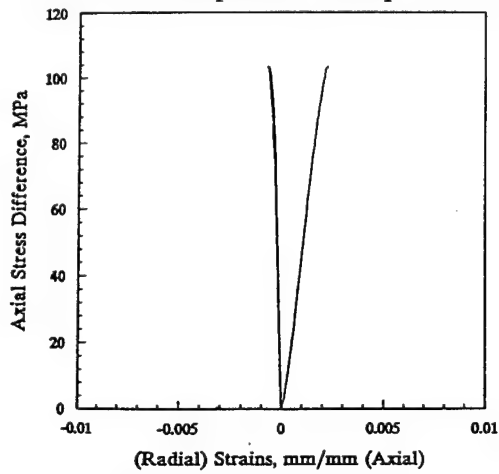
DNA #8A - Parallel
Unconfined Compression - Sample Not Failed



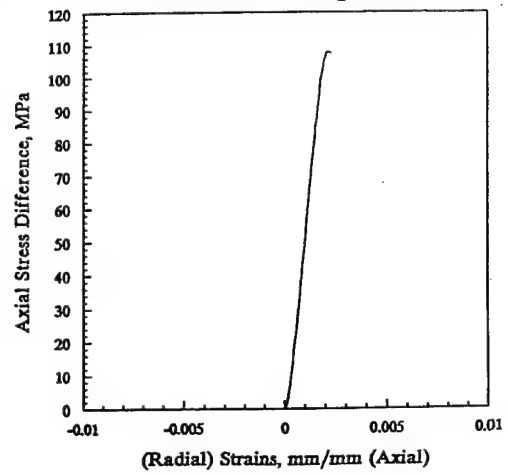
DNA #8A - Parallel
Unconfined Compression



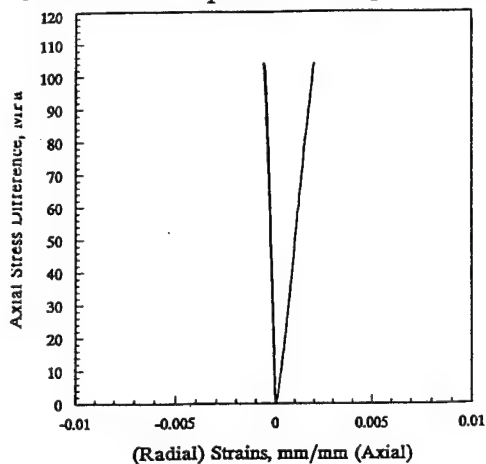
DNA #9A - Parallel
Unconfined Compression - Sample Not Failed



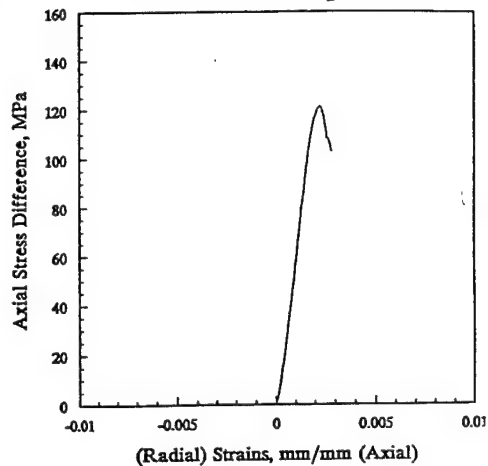
DNA #9A - Parallel
Unconfined Compression



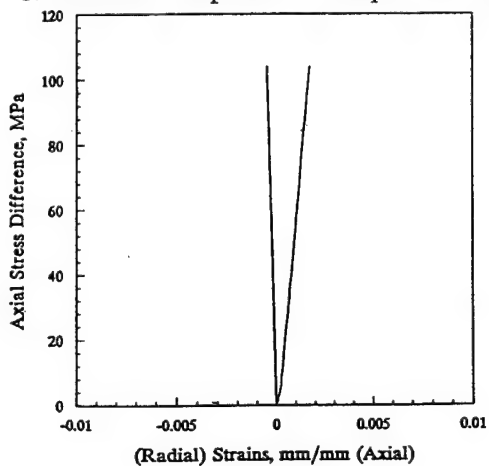
DNA #9C - Perpendicular
Unconfined Compression - Sample Not Failed



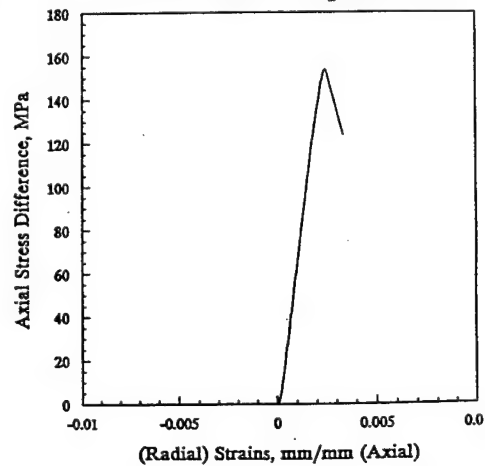
DNA #9C - Perpendicular
Unconfined Compression



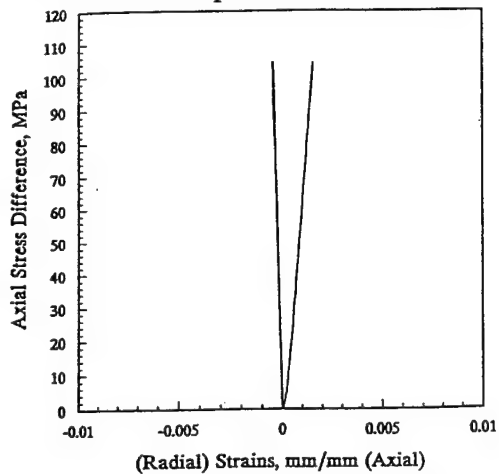
DNA #10A - Parallel
Unconfined Compression - Sample Not Failed



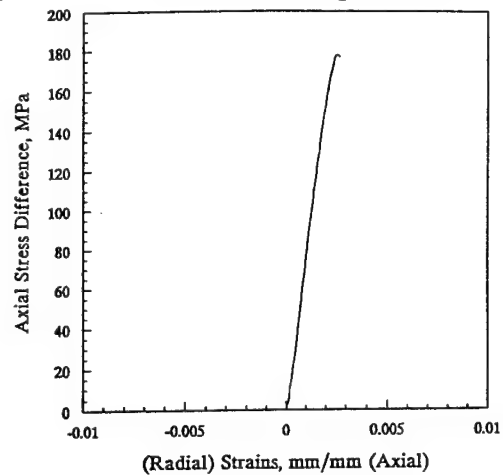
DNA #10A - Parallel
Unconfined Compression



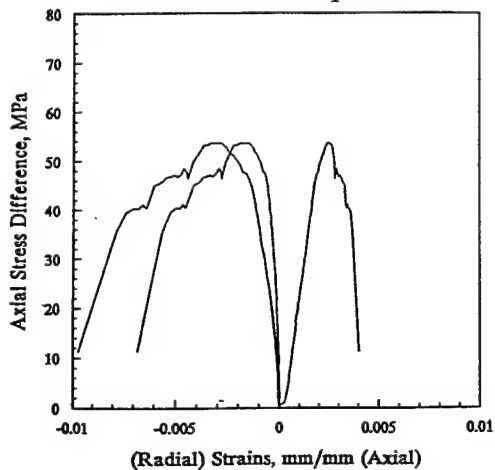
DNA #10C - Perpendicular
Unconfined Compression - Sample Not Failed



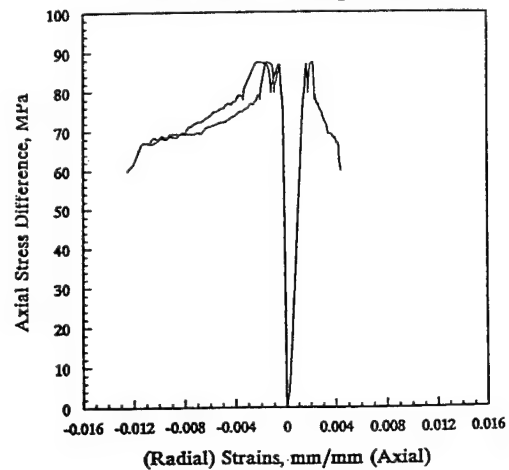
DNA #10C - Perpendicular
Unconfined Compression



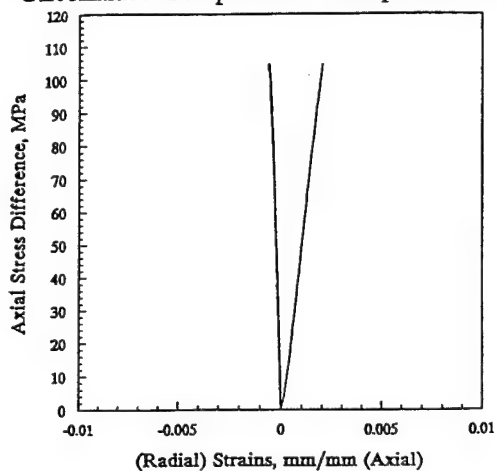
DNA #11A - Parallel
Unconfined Compression



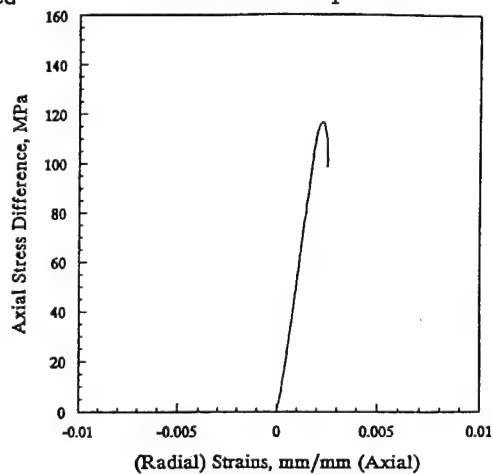
DNA #11C - Perpendicular
Unconfined Compression



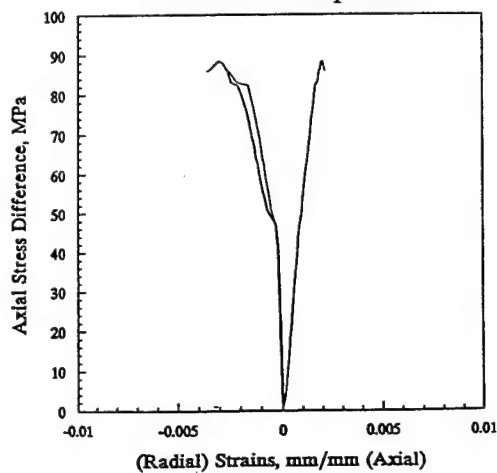
DNA #12A - Parallel
Unconfined Compression - Sample Not Failed



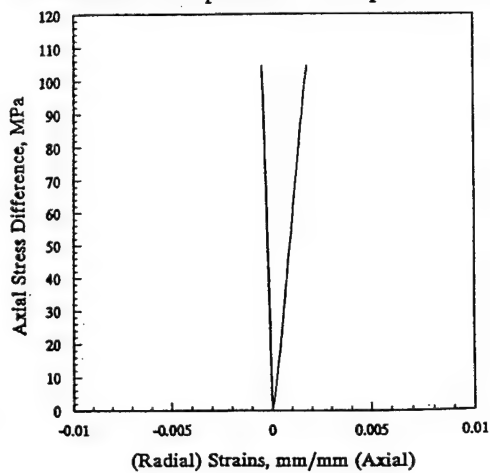
DNA #12A - Parallel
Unconfined Compression



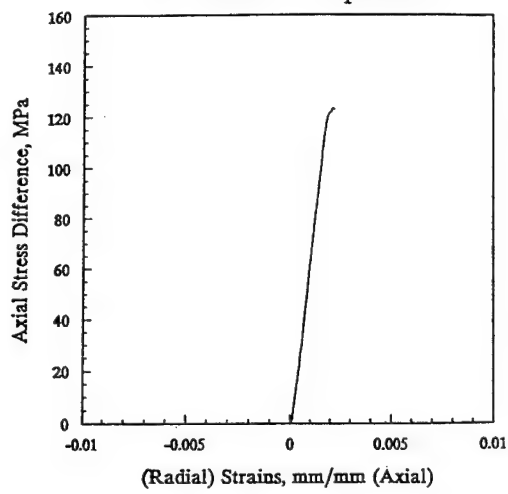
DNA #12C - Perpendicular
Unconfined Compression



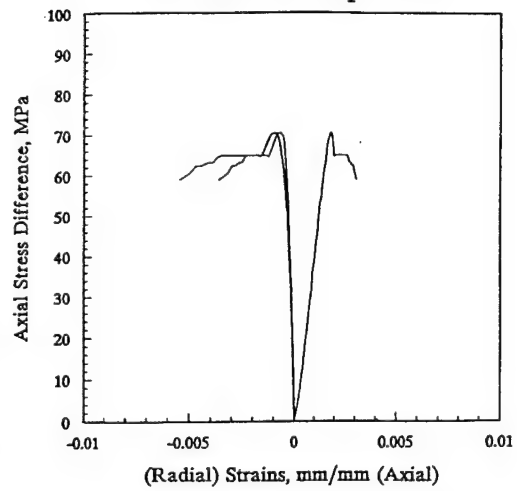
DNA #13A - Parallel
Unconfined Compression - Sample Not Failed



DNA #13A - Parallel
Unconfined Compression

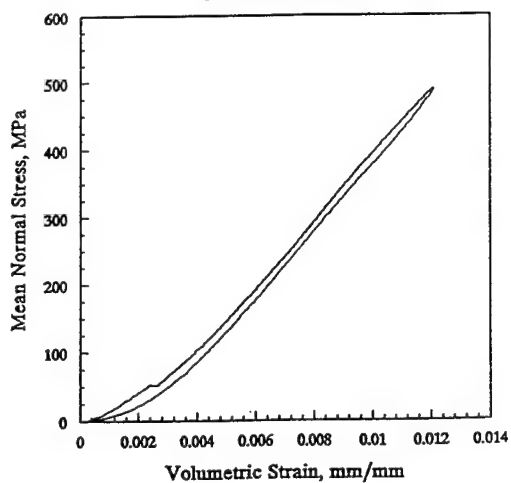


DNA #13C - Perpendicular
Unconfined Compression

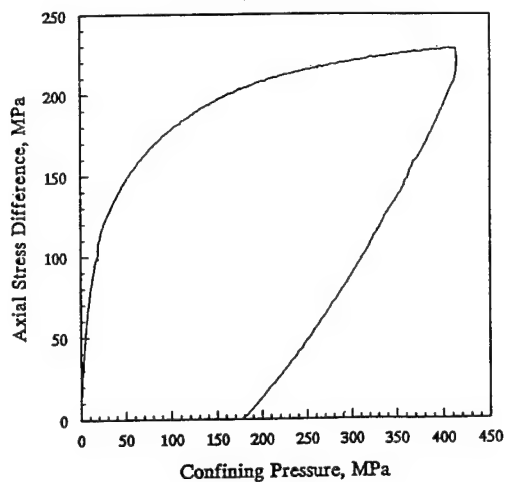


APPENDIX E
UNIAXIAL STRAIN GRAPHICAL PRESENTATIONS

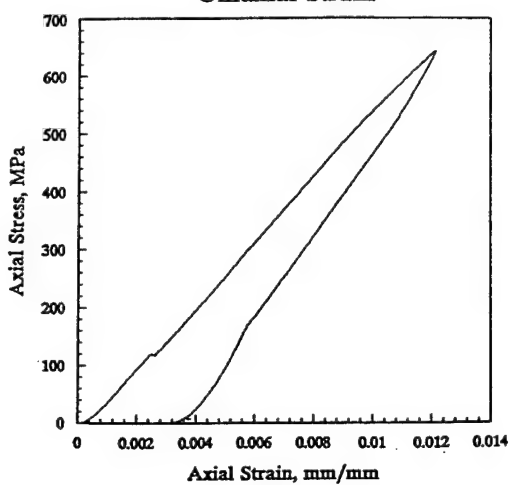
DNA #1B - Parallel
Uniaxial Strain



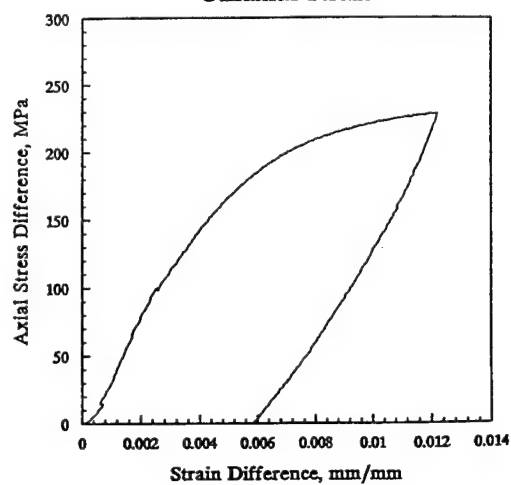
DNA #1B - Parallel
Uniaxial Strain



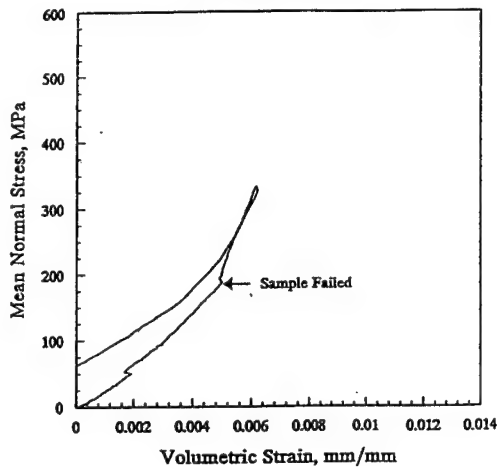
DNA #1B - Parallel
Uniaxial Strain



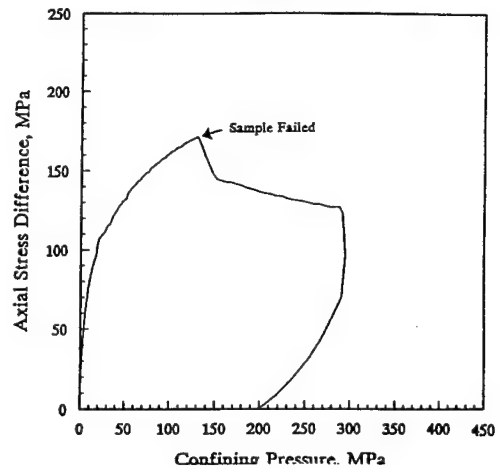
DNA #1B - Parallel
Uniaxial Strain



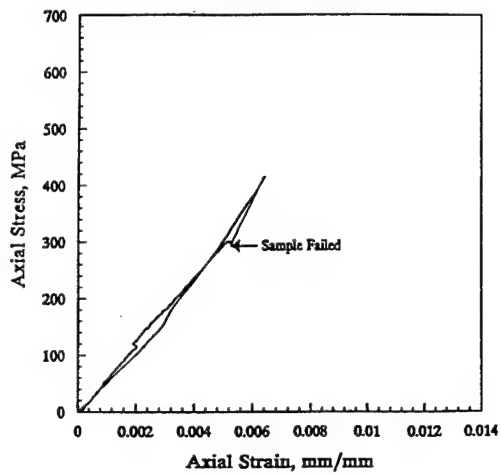
DNA #2A - Parallel
Uniaxial Strain



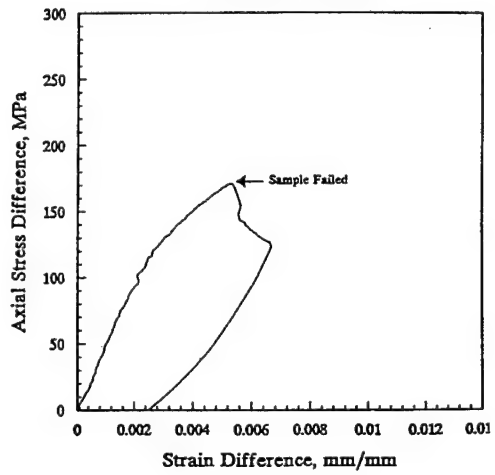
DNA #2A - Parallel
Uniaxial Strain



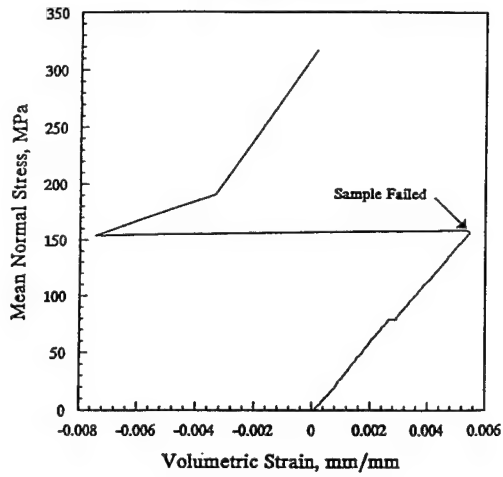
DNA #2A - Parallel
Uniaxial Strain



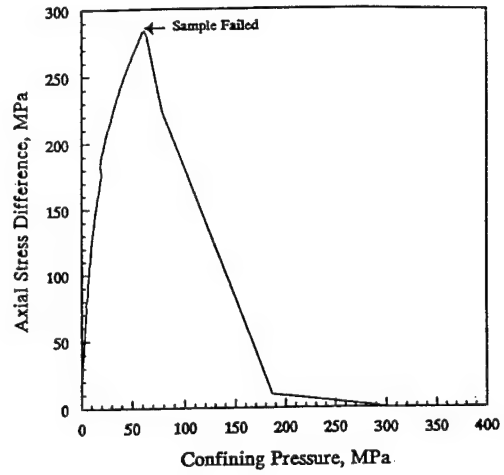
DNA #2A - Parallel
Uniaxial Strain



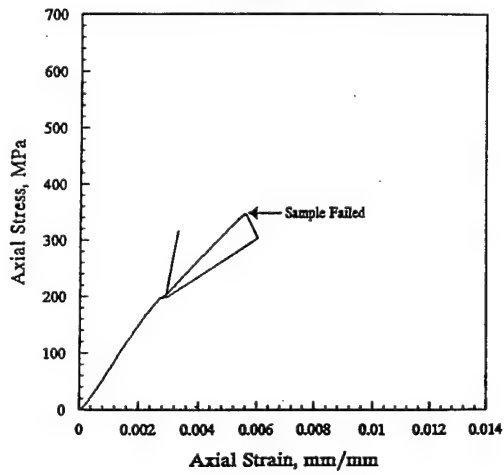
DNA #3B - Parallel
Uniaxial Strain



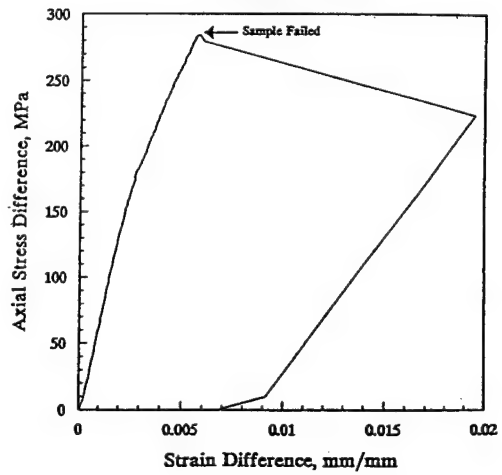
DNA #3B - Parallel
Uniaxial Strain



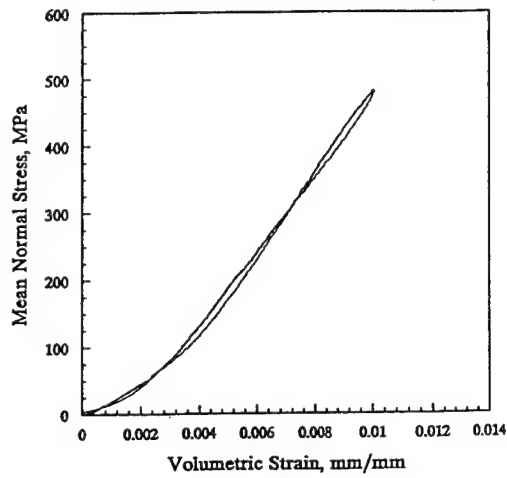
DNA #3B - Parallel
Uniaxial Strain



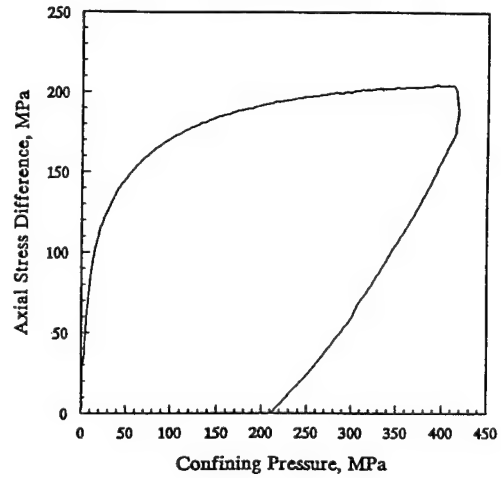
DNA #3B - Parallel
Uniaxial Strain



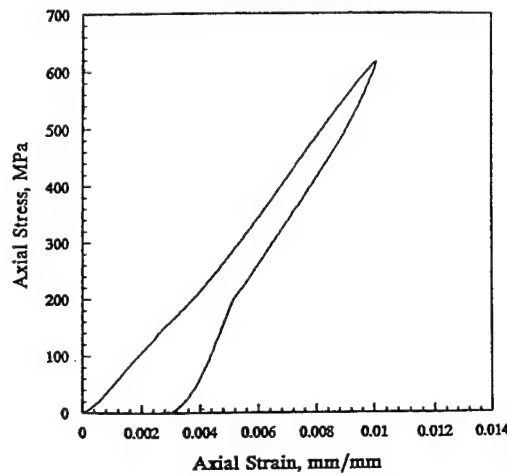
DNA #4B - Parallel
Uniaxial Strain



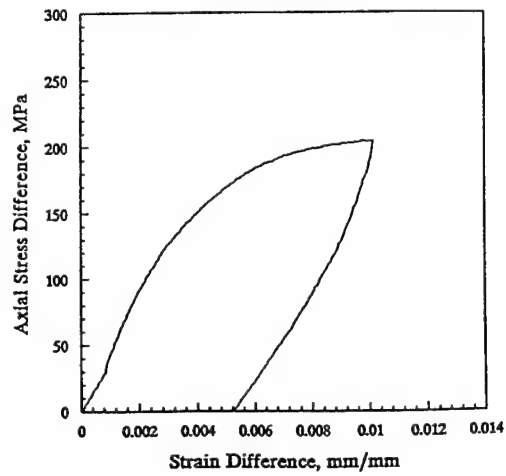
DNA #4B - Parallel
Uniaxial Strain



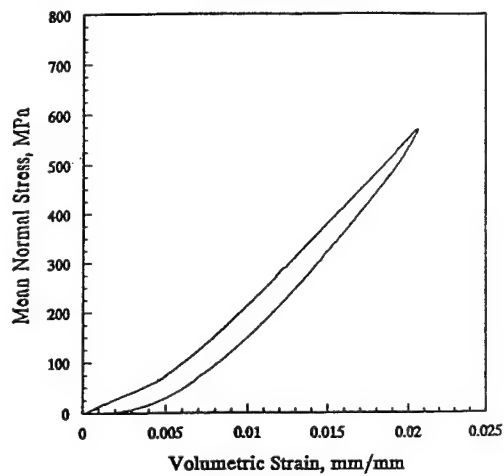
DNA #4B - Parallel
Uniaxial Strain



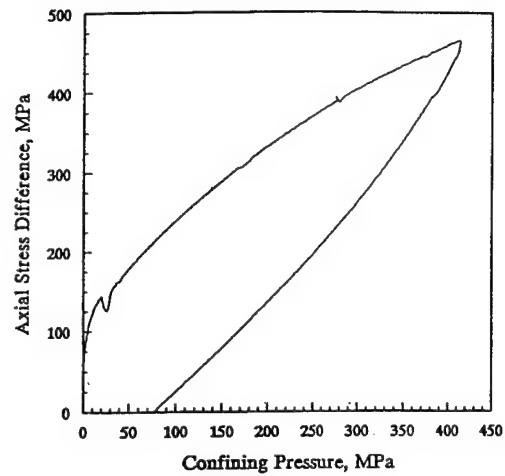
DNA #4B - Parallel
Uniaxial Strain



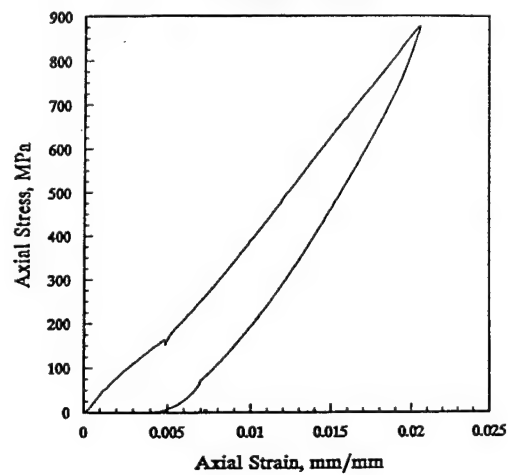
DNA #5B - Parallel
Uniaxial Strain



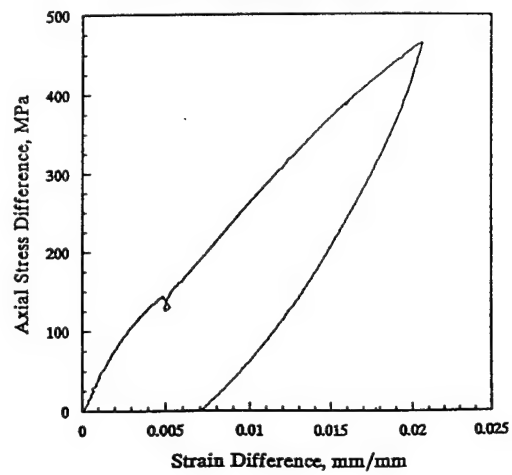
DNA #5B - Parallel
Uniaxial Strain



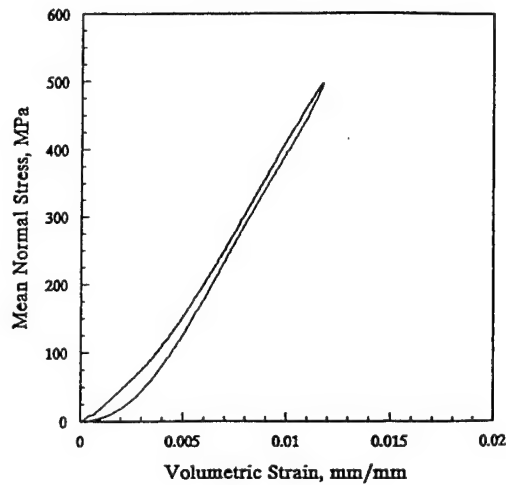
DNA #5B - Parallel
Uniaxial Strain



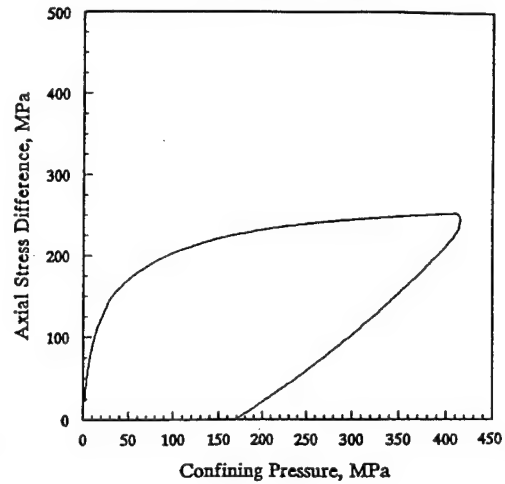
DNA #5B - Parallel
Uniaxial Strain



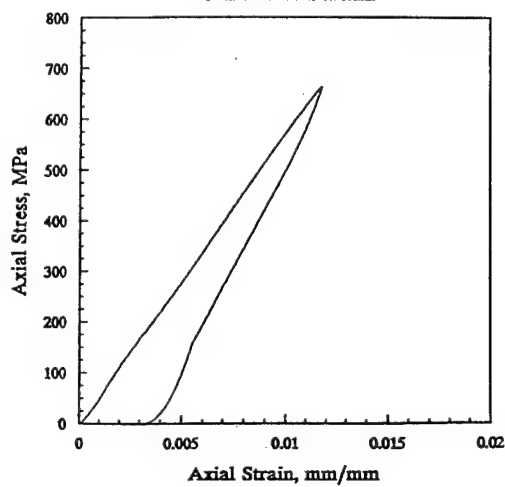
DNA #6B - Parallel
Uniaxial Strain



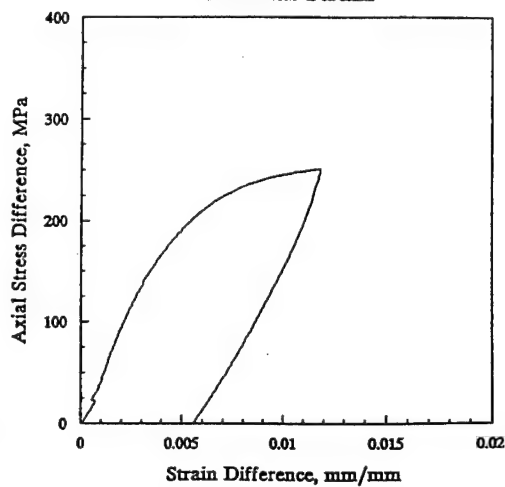
DNA #6B - Parallel
Uniaxial Strain



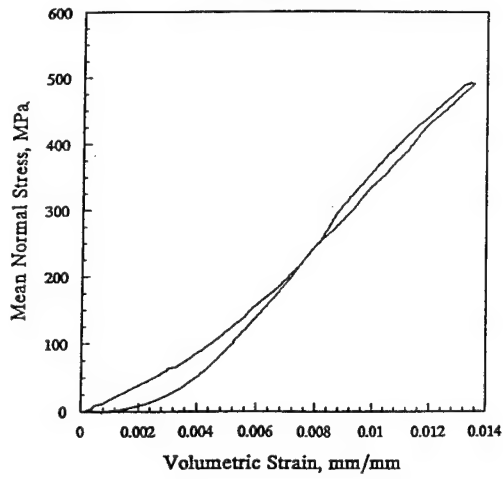
DNA #6B - Parallel
Uniaxial Strain



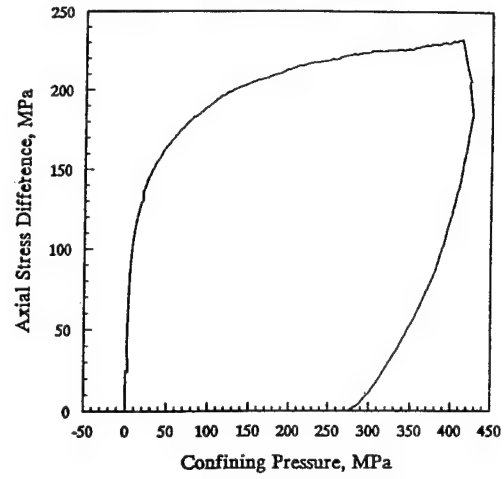
DNA #6B - Parallel
Uniaxial Strain



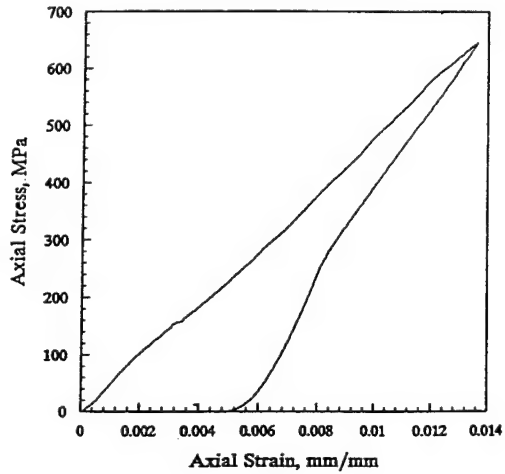
DNA #7B - Parallel
Uniaxial Strain



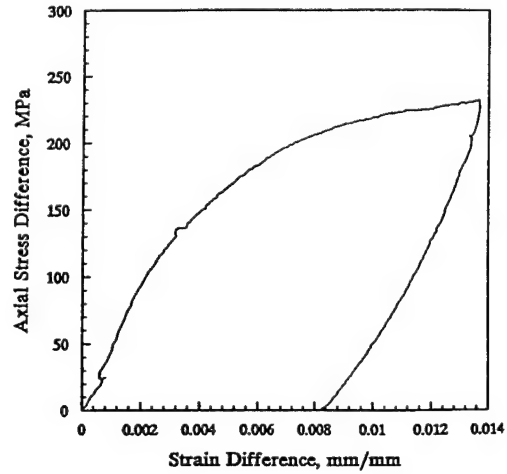
DNA #7B - Parallel
Uniaxial Strain



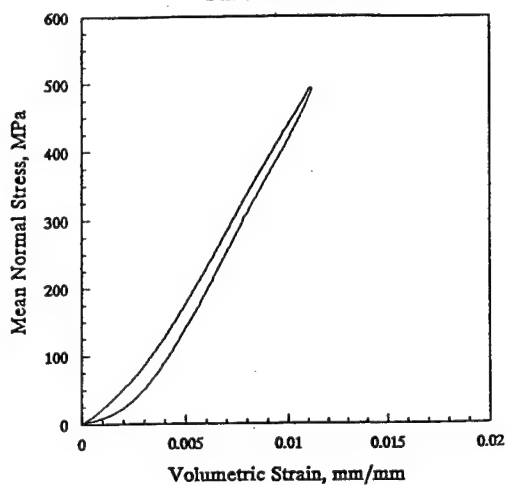
DNA #7B - Parallel
Uniaxial Strain



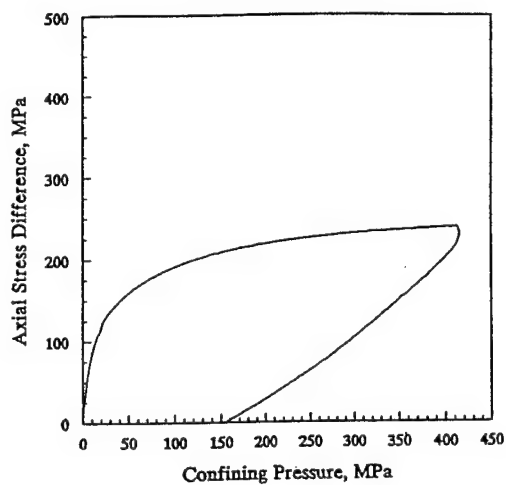
DNA #7B - Parallel
Uniaxial Strain



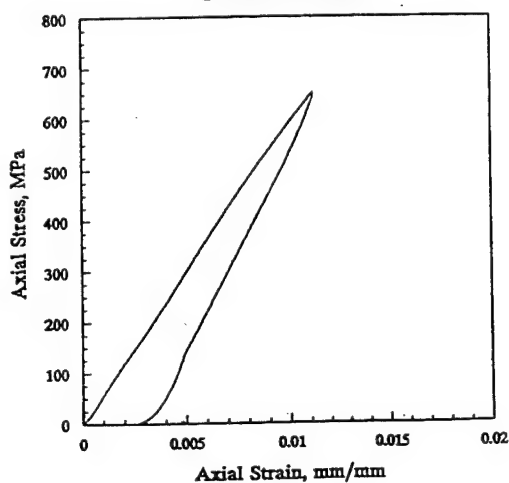
DNA #9B - Parallel
Uniaxial Strain



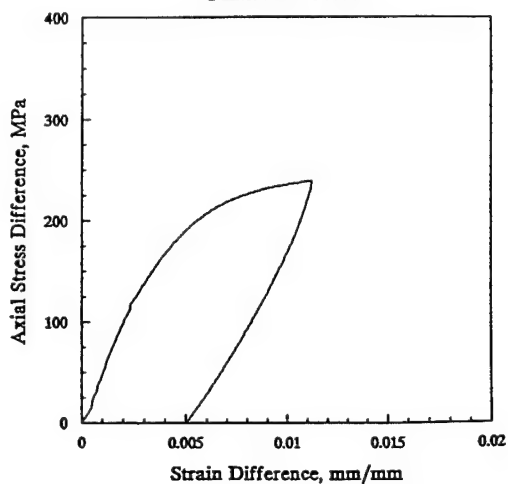
DNA #9B - Parallel
Uniaxial Strain



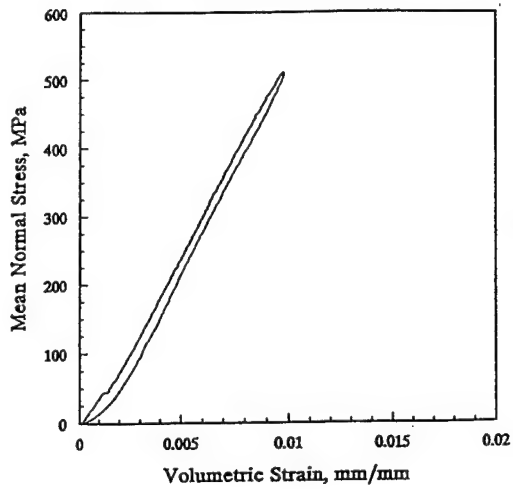
DNA #9B - Parallel
Uniaxial Strain



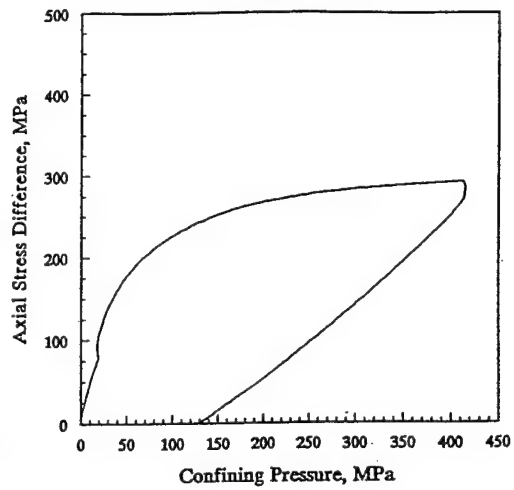
DNA #9B - Parallel
Uniaxial Strain



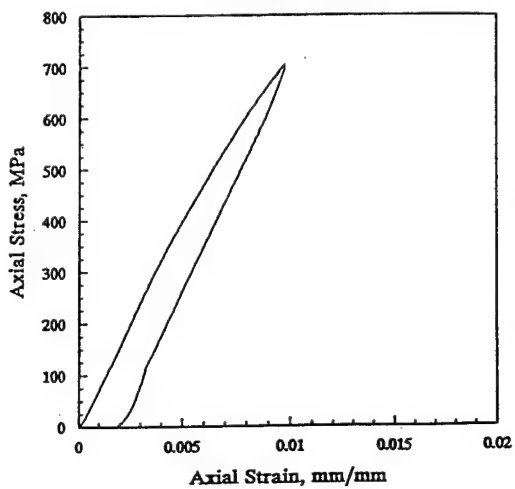
DNA #10B - Parallel
Uniaxial Strain



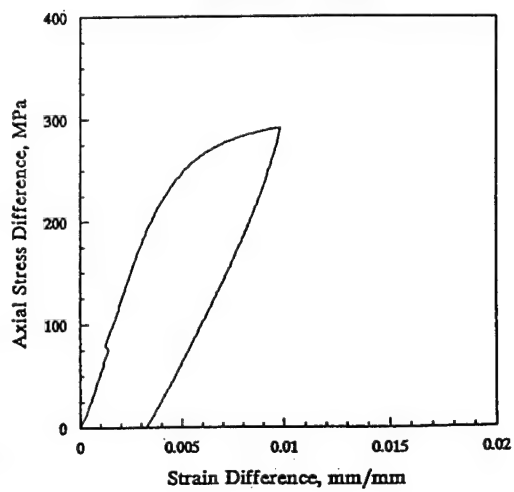
DNA #10B - Parallel
Uniaxial Strain



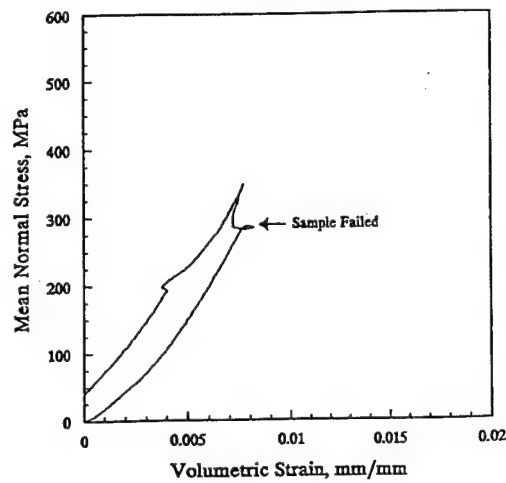
DNA #10B - Parallel
Uniaxial Strain



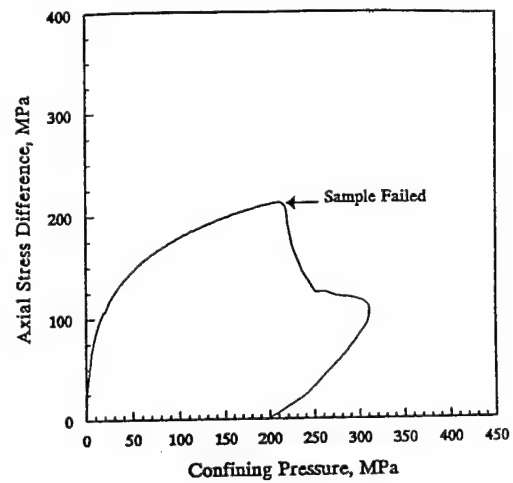
DNA #10B - Parallel
Uniaxial Strain



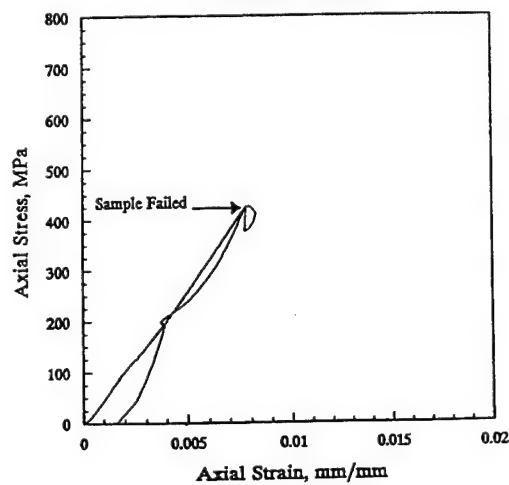
DNA #11B - Parallel
Uniaxial Strain



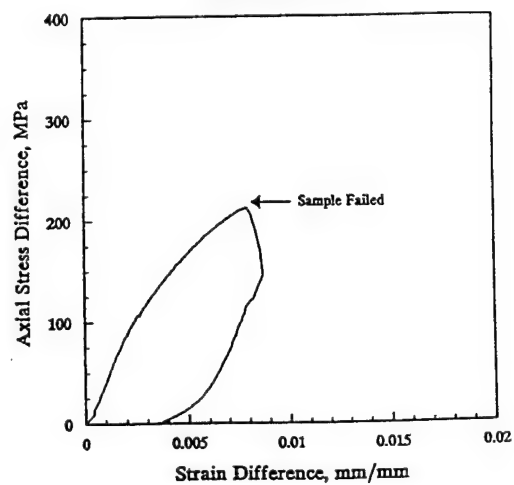
DNA #11B - Parallel
Uniaxial Strain



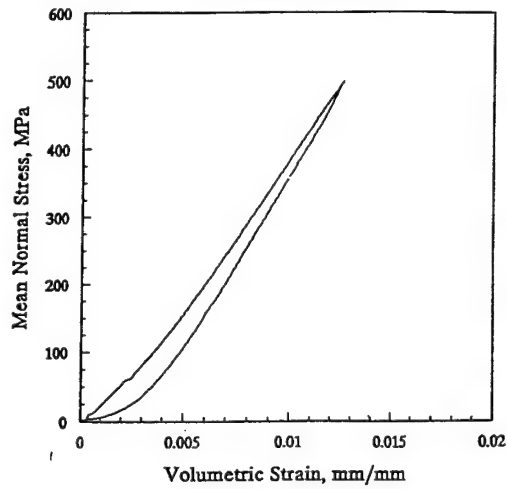
DNA #11B - Parallel
Uniaxial Strain



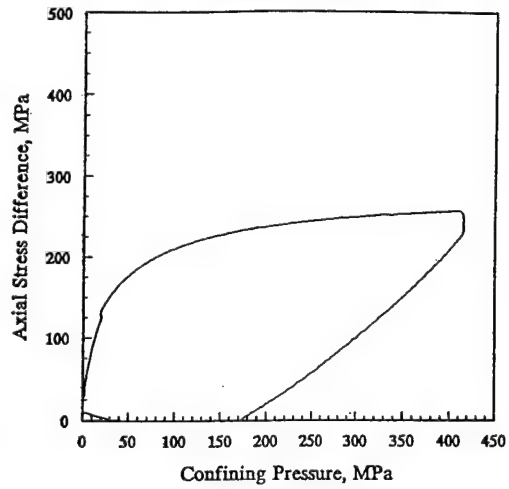
DNA #11B - Parallel
Uniaxial Strain



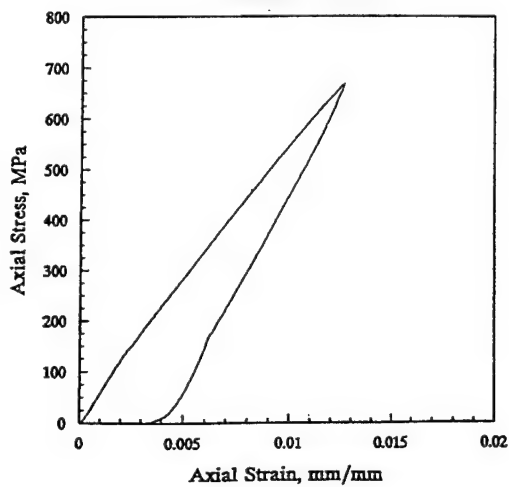
DNA #13B - Parallel
Uniaxial Strain



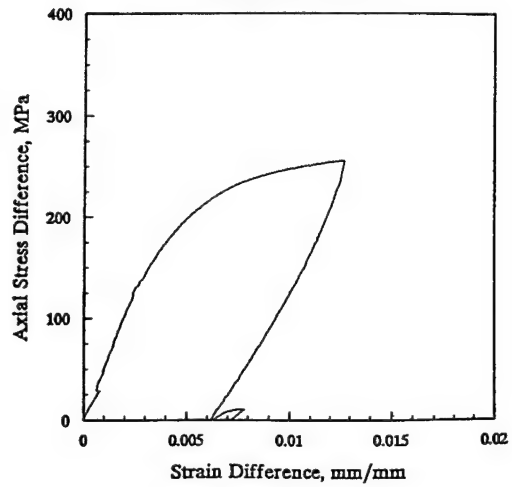
DNA #13B - Parallel
Uniaxial Strain



DNA #13B - Parallel
Uniaxial Strain



DNA #13B - Parallel
Uniaxial Strain



DISTRIBUTION LIST
US/ROK Technical Organizations

<u>No. of Copies</u>	<u>No. of Copies</u>
<p>Commander Office of the Assistant Secretary of the Army (Research, Development & Acquisition) ATTN: SARD-IN 1 RM 3E416 Washington, DC 20310-0103</p>	<p>Chairman Department of Defense Explosives Safety Board ATTN: Technical Library 1 Hoffman Building 1 2461 Eisenhower Avenue Alexandria, VA 22331</p>
<p>Ministry of National Defense Logistics Bureau ATTN: Colonel Yeon Woo Chung 1 1 Yongsan 3ka-dong Yongsan-ku Seoul KOREA 120-023</p>	<p>Applied Research Associates, Inc. ATTN: Mr. Charles Needham 1 Suite A220 4300 San Mateo Blvd., NE Albuquerque, NM 87110</p>
<p>Director U.S. Army Defense Ammunition Center and School ATTN: SMCAC-PMUAST (Mr. Gary Abrisz) 5 Savanna, IL 61074-9639</p>	<p>Agency For Defense Development ATTN: Dr. Song, So-Young 3 ADD 1-3-7 P.O. Box 35 Dae-Jeon, 300-600 REPUBLIC OF KOREA</p>
<p>Chairman Department of Defense Explosives Safety Board ATTN: DDESB-KT (Dr. Chester Canada) 1 2461 Eisenhower Avenue Alexandria, VA 22331-0600</p>	<p>Director Defense Nuclear Agency ATTN: TDTR (Mr. Tom Kennedy) 1 SPWE (Dr. Ed Tremba) 1 SPSD (Dr. K. Goering) 1 6801 Telegraph Road Alexandria, VA 22310-3398</p>
<p>Commander U.S. Army Corps of Engineers Omaha District ATTN: CEMRO-ED-SH (Mr. William Gaube) 1 215 North 17th Street Omaha, NE 68102-4978</p>	<p>Air Force Armaments Laboratory ATTN: ASD/YQI (Mr. J. Jenus) 1 Eglin AFB, FL 32542-5434</p>
<p>Naval Weapons Center Conventional Weapons Division Ordnance Evaluation Department ATTN: Mr. Carl C. Halsey (Code 3269) 1 China Lake, CA 93555-6001</p>	<p>Commander Defense Nuclear Agency ATTN: FCTT (Dr. Byron Ristvit) 1 FCTT (Dr. Eric J. Rinehart) 1 1680 Texas St., SE Kirtland AFB, NM 87117-5669</p>
	<p>Commander Air Warfare Center ATTN: Code 326B (Mr. L. Josephson) 1 China Lake, CA 93555-6001</p>

	<u>No. of Copies</u>		<u>No. of Copies</u>
Commanding Officer Naval Ordnance Station ATTN: Technical Library Indian Head, MD 20640	1	Headquarters, U.S. Air Force ATTN: SEP (Mr. Paul Price) 1400 Air Force Pentagon Washington, DC 20330-1400	1
Commander Belvoir Research, Development and Engineering Center ATTN: AMXME-ND Fort Belvoir, VA 22060	1	Director U.S. Army Research Laboratory ATTN: AMSRL-WT-TB (Mr. John Starkenberg) Aberdeen PG, MD 21005-5066	1
Chief of Engineers Department of the Army ATTN: CERD-ZA 20 Massachusetts Ave. Washington, DC 20314	1	Commander Naval Surface Warfare Center Dahlgren Division ATTN: Code R10H (Mr. Michael Swisdak) 10901 New Hampshire Avenue Silver Spring, MD 20903-5000	1
Southwest Research Institute ATTN: Mr. K. Marchand 8500 Culebra Road San Antonio, TX 78206	1	Commander Naval Facilities Engineering Service Center ATTN: Code ESC-62 (Mr. James Tancreto) Port Hueneme, CA 93043-5003	1
Applied Research Associates ATTN: Mr. J. L. Drake 3202 Wisconsin Ave. Vicksburg, MS 39180	1	Commander Air Force Weapons Laboratory ATTN: NTEDE (Dr. Henny) Kirtland AFB, NM 87117-6008	1
PM AMMOLOG ATTN: AMCPM-AL (Mr. Bob Rossi) Picatinny Arsenal, NJ 07806-5000	1	Director Harry Diamond Laboratories ATTN: SLCHD-NW-RA 2800 Powder Mill Road Adelphi, MD 20783-1197	1
Bakhtar Associates ATTN: Dr. K. Bakhtar 2429 West Coast Highway, Suite 201 Newport Beach, CA 92663	1		
Commander U.S. Army Research Laboratory ATTN: SLCBR-TB-EE (Dr. R. Frey) (Mr. O. Lynn) Aberdeen Proving Ground, MD 21005	1 1		
U.S. Army Corps of Engineers Huntsville Division ATTN: CEHND-ED-CS (Mr. Paul Lahoud) P. O. Box 1600 Huntsville, AL 35807-4301	1		

DISTRIBUTION LIST
Foreign Organizations

	<u>No. of Copies</u>		<u>No. of Copies</u>
Mr. Jacques Besson Ingenieur En Chief De L'Armement Inspection de L'Armement pour les poudres at Explosifs Casernes Sully Place G Clemenceau 10 92211 Saint Cloud Cedex FRANCE	1	Mr. Peter Kummer Bienz, Kummer & Partner Ltd. Langägerstrasse 6 CH 8125 Zollikerberg SWITZERLAND	1
Mr. Martin Kropatschek Bundesministerium der Verlerdigung -Rue T V 5- Postfach 13 28 Federal Republic of GERMANY	1	Mr. Hansjorg E. Rytz GRD-FSFO General Herzog-Haus Ch-3600 Thun 2 SWITZERLAND	1
Mr. Arnfinn Jenssen Chief, Office of Test & Development Norwegian Defence Construction Service Oslo mil/Akershus N-0015 Oslo 1 NORWAY	1	Defence Research Establishment Suffield Military Engineering Section ATTN: Mr. David Ritzel Ralston, Alberta T0J 2N0 CANADA	1
Dr. Bengt Vretblad Royal Swedish Fortifications Administration, Research Department S-63189, Eskilstuna SWEDEN	1	Norwegian Defence Research Establishment ATTN: Mr. Svein Rollvik P. O. Box 25 N-2007 Kjeller NORWAY	1
Mr. Jon Henderson Ministry of Defence Directorate of Defence Health and Safety "Aquila" Golf Road BROMLEY, BR1 2JB ENGLAND	1		

REPORT DOCUMENTATION PAGE

Form Approved
OMB No. 0704-0188

Public reporting burden for this collection of information is estimated to average 1 hour per response, including the time for reviewing instructions, searching existing data sources, gathering and maintaining the data needed, and completing and reviewing the collection of information. Send comments regarding this burden estimate or any other aspect of this collection of information, including suggestions for reducing this burden, to Washington Headquarters Services, Directorate for Information Operations and Reports, 1215 Jefferson Davis Highway, Suite 1204, Arlington, VA 22202-4302, and to the Office of Management and Budget, Paperwork Reduction Project (0704-0188), Washington, DC 20503.

1. AGENCY USE ONLY (Leave blank)		2. REPORT DATE September 1996		3. REPORT TYPE AND DATES COVERED Final report	
4. TITLE AND SUBTITLE Material Characterization of Samples from the Lynchburg Mine				5. FUNDING NUMBERS UAST-CR-94-007 DACA39-92-R-0063	
6. AUTHOR(S) J. Wesley Martin					
7. PERFORMING ORGANIZATION NAME(S) AND ADDRESS(ES) TerraTek, Inc. P. O. Box 8275 Salt Lake City, UT 84108-8275				8. PERFORMING ORGANIZATION REPORT NUMBER Contract Report SL-96-3	
9. SPONSORING/MONITORING AGENCY NAME(S) AND ADDRESS(ES) U.S. Army Corps of Engineers Washington, DC 20314-1000 U.S. Army Engineer Waterways Experiment Station 3909 Halls Ferry Road, Vicksburg, MS 39180-6199				10. SPONSORING/MONITORING AGENCY REPORT NUMBER	
11. SUPPLEMENTARY NOTES Available from National Technical Information Service, 5285 Fort Royal Road, Springfield, VA 22161.					
12a. DISTRIBUTION/AVAILABILITY STATEMENT Approved for public release; distribution is unlimited.				12b. DISTRIBUTION CODE	
13. ABSTRACT (Maximum 200 words) Laboratory tests were conducted on predominantly limestone core samples from the Lynchburg Mine near Magdalena, NM. The core samples were retrieved from horizontal drill holes located in test chambers and drifts. Tests were conducted on the core samples to characterize the material. This included lithologic descriptions, physical property measurements, ultrasonic velocity measurements, uniaxial compression tests, and uniaxial strain.					
14. SUBJECT TERMS Limestone Uniaxial compression Lithology Uniaxial strain Physical properties Ultrasonic velocity				15. NUMBER OF PAGES 82	
				16. PRICE CODE	
17. SECURITY CLASSIFICATION OF REPORT UNCLASSIFIED	18. SECURITY CLASSIFICATION OF THIS PAGE UNCLASSIFIED	19. SECURITY CLASSIFICATION OF ABSTRACT		20. LIMITATION OF ABSTRACT	